



# JGR Atmospheres

## RESEARCH ARTICLE

10.1029/2020JD033324

### Key Points:

- An initially large vortex can expand more quickly than its relatively smaller counterpart
- Outer-core convection exhibits a scale-dependent response to varying the incipient vortex circulation
- Increasing the environmental moisture promotes expansion but mostly expedites the intensification process

### Correspondence to:

J. Martinez,

[jon.martinez@colostate.edu](mailto:jon.martinez@colostate.edu)

### Citation:

Martinez, J., Nam, C. C., & Bell, M. M. (2020). On the contributions of incipient vortex circulation and environmental moisture to tropical cyclone expansion. *Journal of Geophysical Research: Atmospheres*, 125, e2020JD033324. <https://doi.org/10.1029/2020JD033324>

Received 17 JUN 2020

Accepted 11 OCT 2020

Accepted article online 18 OCT 2020

## On the Contributions of Incipient Vortex Circulation and Environmental Moisture to Tropical Cyclone Expansion

Jonathan Martinez<sup>1</sup> , Chaehyeon Chelsea Nam<sup>1</sup> , and Michael M. Bell<sup>1</sup>

<sup>1</sup>Department of Atmospheric Science, Colorado State University, Fort Collins, CO, USA

**Abstract** This study investigates the contributions of incipient vortex circulation and midlevel moisture to tropical cyclone (TC) expansion within an idealized numerical modeling framework. We find that the incipient vortex circulation places the primary constraint on TC expansion. Increasing the midlevel moisture further promotes expansion but mostly expedites the intensification process. The expansion rate for initially large vortices exhibits a stronger response to increasing the midlevel moisture compared to initially small vortices. Previous studies have noted a proclivity for relatively small TCs to stay small and relatively large TCs to stay large; that is, TCs possess a sort of “memory” with respect to their incipient circulation. We reproduce this finding with an independent modeling framework and further demonstrate that an initially large vortex can expand more quickly than its relatively smaller counterpart; therefore, with all other factors contributing to expansion held constant, the contrast in size between the two vortices will increase with time. Varying the incipient vortex circulation is associated with subsequent variations in the amount and scale of outer-core convection. As the incipient vortex circulation decreases, outer-core convection is relatively scarce and characterized by small-scale, isolated convective elements. On the contrary, as the incipient vortex circulation increases, outer-core convection abounds and is characterized by relatively large rainbands and mesoscale convective systems. A combined increase in the amount and scale of outer-core convection permits an initially large vortex to converge a substantially greater amount of absolute angular momentum compared to its relatively smaller counterpart, resulting in distinct expansion rates.

**Plain Language Summary** A variety of atmospheric and oceanic processes contribute to the expansion of a tropical cyclone wind field. We examine a subset of factors with idealized simulations to better understand how tropical cyclones expand. When both the initial size of a tropical cyclone and the environmental moisture are varied in accordance with observations, we find that the initial size of a tropical cyclone places the primary constraint on the expansion of a tropical cyclone wind field. We verify that tropical cyclones possess “memory” of their size when they first developed such that a small tropical cyclone stays small and a large tropical cyclone stays large. We further demonstrate that large tropical cyclones can expand more quickly than their relatively smaller counterparts. The amount of moisture in the atmosphere modulates the expansion of a tropical cyclone wind field. A relatively moist environment facilitates the development of convection and a concomitant increase of wind speeds that contributes to an expansion of the tropical cyclone wind field. Our findings motivate additional research investigating the variability of processes contributing to the initial size of a tropical cyclone amidst Earth’s warming climate system.

### 1. Introduction

Accurately forecasting the lateral extent of a tropical cyclone (TC) wind field provides critical information to assess the potential scope of its wind, precipitation, and storm surge-related hazards. Climatological studies have shown that TCs are characterized by an expansive range of scales (Chan & Chan, 2012; Chavas & Emanuel, 2010; Knaff et al., 2014; Merrill, 1984); however, the processes contributing to variable TC sizes are not fully understood. Complex multiscale interactions occurring between a TC and its ambient environment underlie the difficulties associated with accurately forecasting the lateral expansion of a TC wind field. Several risk analyses have demonstrated the importance of considering TC size metrics in assessing the potential amount of losses associated with landfalling TCs (e.g., Czajkowski & Done, 2014; Klotzbach et al., 2020; Powell & Reinhold, 2007; Wang & Toumi, 2016; Zhai & Jiang, 2014). Furthermore, recent studies have demonstrated that TC size distributions among various ocean basins will shift toward larger TCs amidst

Earth's warming climate system (Knutson et al., 2015). As societal exposure to TC hazards continues to escalate among expanding coastal communities (Klotzbach et al., 2018), a thorough understanding of the processes contributing to the lateral expansion of TC wind fields is necessary to prevent fatalities and mitigate economic losses.

In proceeding, we note that several metrics of "size" exist in the literature, each describing to varying degrees the lateral extent of the TC circulation. Rather than elaborating the utility of each metric, we will note a few among the more commonly employed in the literature and refer the reader to a subset of references listed below: Radius of the outermost closed surface isobar (ROCI; Brand, 1972; Kimball & Mulekar, 2004; Merrill, 1984), radius of hurricane-force winds (64 kt Hill & Lackmann, 2009), radius of damaging-force winds (50 kt Kimball & Mulekar, 2004; Xu & Wang, 2010), and the equivalent radii of tropical storm force and gale force winds (34 kt Chan & Chan, 2012; Kilroy & Smith, 2017). Operational forecasting agencies, such as the National Hurricane Center and the Joint Typhoon Warning Center, routinely produce wind radii forecasts for the radius of hurricane-force winds, damaging-force winds, and tropical storm force winds (Knaff et al., 2017). Following Kilroy and Smith (2017), we define TC size as the maximum extent of the azimuthally averaged tangential velocity equal to the radius of gale force winds (34 kt) 1 km above the ocean surface (henceforth,  $R_{gales}$ ). Furthermore, we define TC expansion as the process whereby  $R_{gales}$  increases and conversely, contraction as the process whereby  $R_{gales}$  decreases.

The two tails of the global TC size distribution represent vastly different scales, demonstrating the potential for TCs to exhibit remarkable structural differences. Early studies provided evidence for weak typhoons with compact circulations, referred to as "midget" typhoons (Arakawa, 1952; Harr et al., 1996). On the same tail of the TC size distribution are intense TCs with compact circulations, referred to as "microhurricanes" (Hawkins & Rubsam, 1966) or "strong dwarfs" when depicted on an intensity-kinetic energy diagram (Musgrave et al., 2012). Exemplars of intense TCs with compact circulations include Hurricane Inez (1966 Hawkins & Imbembo, 1976; Hawkins & Rubsam, 1966) and Hurricane Patricia (2015 Doyle et al., 2017; Martinez et al., 2019; Rogers et al., 2017). The opposite tail of the TC size distribution is characterized by TCs such as Super Typhoon Tip (1979), which at its most intense stage possessed a maximum sustained wind speed of  $\sim 85 \text{ m s}^{-1}$  and a radius of gale force winds exceeding 1,100 km (Dunnavan & Diercks, 1980). Together, the foregoing examples allude to the weak relationship between TC intensity and size (Carrasco et al., 2014; Merrill, 1984; Weatherford & Gray, 1988). Such profound differences in TC size further emphasize the difficulties in forecasting potential hazards as a TC approaches land, necessitating a better understanding of expansion at various stages during a TC's life cycle.

Interbasin comparisons have demonstrated that TCs in the western North Pacific basin, on average, tend to be the largest (Knaff et al., 2014; Merrill, 1984). Seasonal variations in TC size have been noted in the North Atlantic and western North Pacific basins, with average sizes exhibiting a relative minimum during midsummer months and a relative maximum during the fall (Brand, 1972; Kimball & Mulekar, 2004; Liu & Chan, 2002; Merrill, 1984). Although basin and season alone do not necessarily provide physical information to describe TC size differences, interbasin and seasonal variations in mesosynoptic scale precursor disturbances to cyclogenesis and environmental conditions, such as sea surface temperatures and moisture, are certainly among the many factors underlying observed differences in TC size. For example, Knaff et al. (2014) concluded that small TCs are favored when vertical vorticity is supplied by the incipient vortex disturbance rather than the synoptic environment. Liu and Chan (2002) found that large TCs in the western North Pacific tend to be associated with a southwesterly surge of environmental flow into the vortex at 850 hPa resulting from cross-equatorial monsoonal flow, whereas small TCs tend to be embedded within easterly flow. Congruous with the foregoing discussion, variance in TC size can be partly attributed to the scale of an incipient vortex and the ambient large-scale environment throughout a TC's life cycle.

Idealized modeling studies have sought to elucidate the most relevant processes governing TC expansion. Hill and Lackmann (2009) demonstrated that environmental humidity is an important factor contributing to TC size. Increasing the environmental humidity promotes a greater amount of PV generated by radially outward propagating spiral rainbands. PV generated by the spiral rainbands is then subsumed by the inner-core PV tower, increasing its lateral extent and spinning up the outer-core cyclonic wind field through a balanced response. Wang and Toumi (2019) demonstrated that artificially reducing the midlevel moisture surrounding a TC circulation can enhance the radial gradient of diabatic heating in the outer-core region

and subsequently promote an expansion of the vortex through a balanced secondary circulation response. Xu and Wang (2010) demonstrated that increasing the RMW of incipient vortices results in larger outer-core surface fluxes that promote stronger diabatic heating within spiral rainbands. Stronger diabatic heating within spiral rainbands promotes more boundary layer vorticity convergence that spins up the outer-core circulation, which in turn increases the surface fluxes at increasingly larger radii. Xu and Wang (2010) also demonstrated that varying the RMW of incipient vortices has a larger influence on the final size of a TC compared to varying the environmental moisture. Chan and Chan (2014) demonstrated that TC size exhibits a dependency on both initial vortex size and planetary vorticity. They argued that when holding the vortex size constant, angular momentum fluxes imparted by the Coriolis torque increase when displacing the vortex further north, whereas radial fluxes of relative angular momentum decrease as a result of increased inertial stability. These competing effects on angular momentum fluxes were shown to be minimized at 25°N such that there may exist an “optimal” latitude for TC expansion. Chan and Chan (2015) demonstrated that TC expansion rates are not sensitive to the initial vortex intensity, but rather TC expansion rates exhibit sensitivity to the outer-core wind profile radially outward of the RMW. Broadening the outer-core tangential wind profile produces a greater amount of absolute angular momentum that can be subsequently converged toward the TC center, thereby promoting quicker expansion rates. Kilroy and Smith (2017) emphasized the importance of boundary layer dynamics in governing both the radial location of low-level ascent out of the boundary layer and the associated thermodynamic properties of this air. They demonstrated with the aid of a slab boundary layer model that an initially large vortex concentrates relatively weak ascent over a broad radial region near the axis of rotation compared to an initially small vortex that concentrates relatively strong ascent closer to the axis of rotation. The organization of ascent occurs prior to the development of deep convection. A larger vortex will therefore develop a broader distribution of diabatic heating and stronger inflow at larger radii, which in the presence of a larger radial absolute angular momentum gradient contributes to a more rapid spin-up of the outer-core circulation. A reasonable conclusion drawn from idealized modeling studies in aggregate is that TC expansion is inextricably linked to convectively driven convergence of absolute angular momentum toward the TC center of circulation.

The foregoing discussion demonstrates there are several internal and external factors contributing to TC expansion; however, our understanding of how these factors evolve together and contribute to TC expansion remains limited. In nature, “internal” and “external” factors are not entirely independent, precluding definitive statements regarding the relative contributions of one factor in one category over the other. Furthermore, employing a combined framework that integrates both internal and external factors is challenging and requires selecting from the numerous potential factors contributing to TC expansion in each respective category. Therefore, it is practical to limit the number of factors we explore and to investigate the underlying processes contributing to TC expansion associated with this reduced set of factors. Here we choose to examine the contributions of incipient vortex circulation and environmental moisture to TC expansion; that is, one “internal” and one “external” factor, respectively. Our choice is motivated by the aforementioned relevance of the incipient vortex circulation and environmental moisture when considering TC expansion.

Several past studies have noted a proclivity for relatively small TCs to stay small and relatively large TCs to stay large (e.g., Kilroy & Smith, 2017; Knaff et al., 2014; Merrill, 1984; Tao et al., 2020). The results presented herein reproduce this finding and indicate potential for additional, new insights regarding TC expansion. The following section discusses the methods to create variable incipient vortex circulations and environmental moisture profiles within the idealized numerical modeling framework. Section 3 presents results gathered from the simulations. Section 4 discusses the underlying processes contributing to TC expansion and avenues for future work, and section 5 provides concluding remarks.

## 2. Methods

### 2.1. Incipient Vortex Circulation

Previous studies investigating the contributions of initial vortex size to TC expansion within an idealized modeling framework begin by prescribing an axisymmetric vortex profile with a fixed tangential velocity maximum. A subset of vortices with different sizes is created by either varying the radius of maximum tangential winds (RMW; e.g., Kilroy & Smith, 2017; Xu & Wang, 2010, 2018) or fixing the RMW and varying the

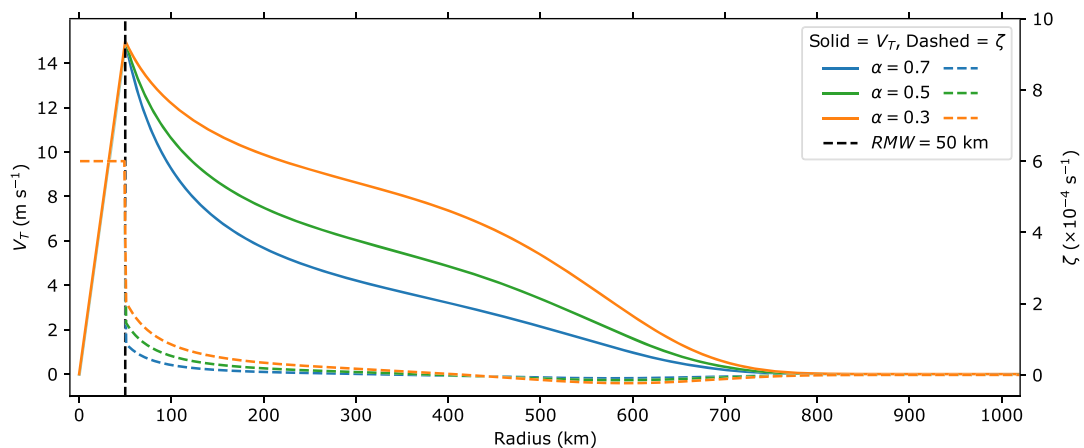


**Figure 1.** Axisymmetric radial profiles of tangential velocity (solid) and vertical vorticity (dashed) are shown for each of the incipient vortices. The decay parameter used for each modified Rankine vortex is given in the legend by  $\alpha$ . A radial decay function (2) is applied to each of the tangential velocity profiles to ensure that the total circulation is zero in the doubly periodic model domain for 3-D simulations. See section 2.3 for additional details.

radial vortex shape outward of the RMW (e.g., Chan & Chan, 2014, 2015; Xu & Wang, 2018). Although the two methods vary a different element of the incipient vortex circulation, and thus likely differ in producing variable TC expansion rates, both methods more generally vary the incipient vortex circulation strength. That is, either increasing the RMW or decreasing the radial decay of tangential velocity outward of the RMW is tantamount to increasing the incipient vortex circulation strength.

We choose to fix the initial tangential velocity maximum and RMW while varying the radial decay of tangential velocity outward of the RMW to produce a set of incipient vortices. The radial structure of tangential velocity is prescribed via a modified Rankine vortex of the form

$$v(r) = \begin{cases} v_{\max} \left( \frac{r}{r_{\max}} \right) & 0 \leq r < r_{\max} \\ v_{\max} \left( \frac{r}{r_{\max}} \right)^{-\alpha} & r \geq r_{\max}, \end{cases} \quad (1)$$

where  $v_{\max} = 15 \text{ m s}^{-1}$  is the maximum tangential velocity,  $r_{\max} = 50 \text{ km}$  is the RMW, and  $\alpha$  is the decay parameter. After the radial structure of the incipient vortices is prescribed, we apply a radial decay function following Nolan (2007) to ensure that the total circulation is zero in the doubly periodic model domain for 3-D simulations. The radial decay function is given by

$$v(r) = v_0(r) \exp\left(-\frac{r}{R}\right), \quad (2)$$

where  $v_0(r)$  denotes the initial modified Rankine vortex profile given by (1),  $r$  is the radius, and  $R$  is chosen as 600 km. Figure 1 shows the tangential velocity and vorticity profiles after applying the radial decay function. Then, a linear vertical decay function is applied that reduces the tangential velocity to zero at an altitude of 20 km. Values of  $\alpha$  are chosen as 0.3, 0.5, and 0.7, in accordance with observations of North Atlantic basin TCs (Mallen et al., 2005). It is unlikely that a tropical storm is characterized by as steep a radial decay of tangential velocity given by the  $\alpha = 0.7$  vortex, but we examine this subset of vortices to elucidate the contributions of incipient vortex circulation to TC expansion. The  $\alpha = 0.7$  and  $\alpha = 0.3$  vortices will henceforth be referred to as small and large, respectively.

## 2.2. Environmental Moisture

The degree to which environmental moisture modulates TC expansion will strongly depend on its horizontal and vertical variations throughout the atmosphere. Prior studies investigating the contributions of environmental moisture to TC expansion often designate a sounding representative of the tropics, fix the

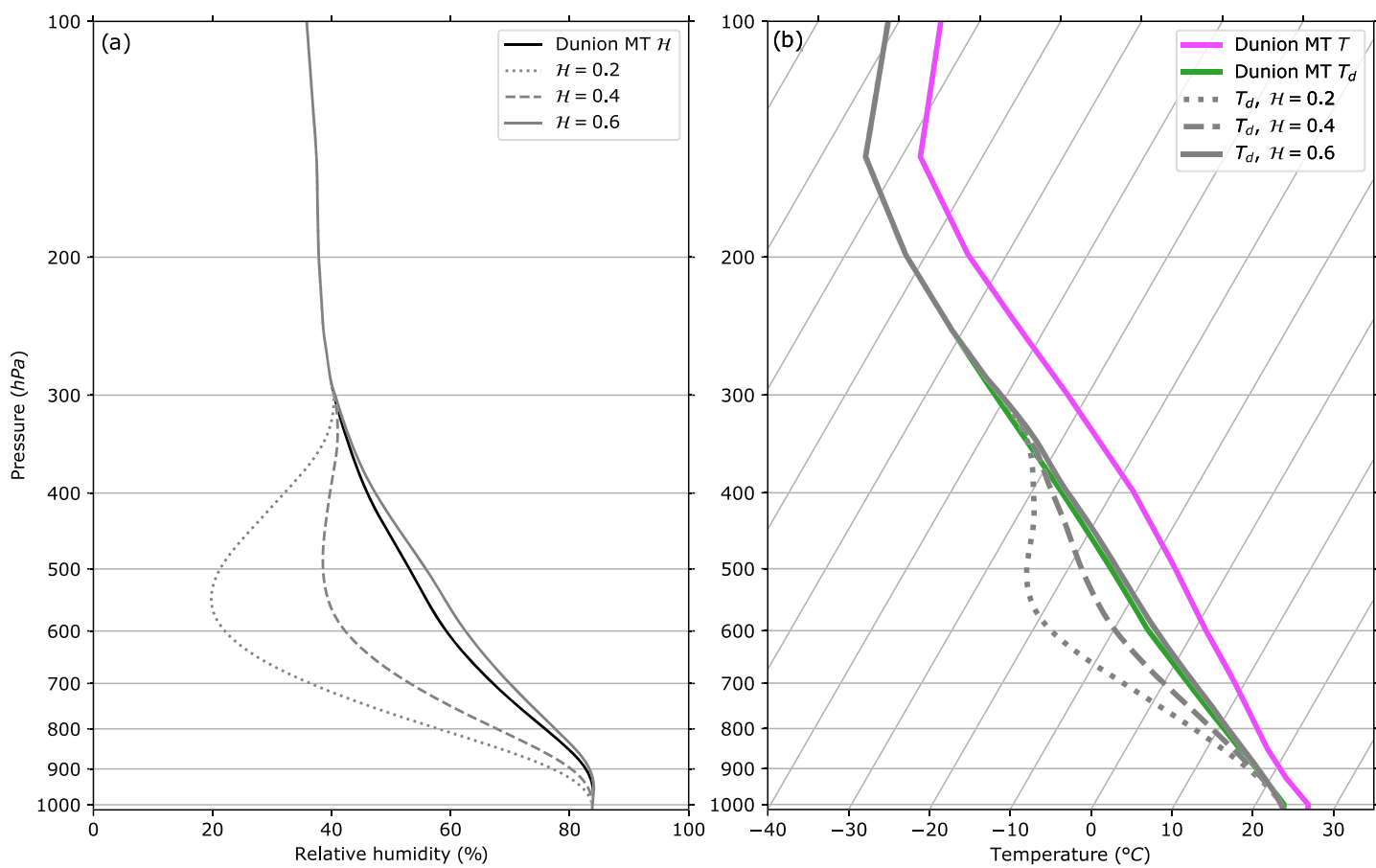


**Figure 2.** (a) Relative humidity ( $\mathcal{H}$ ) is shown as a function of log-pressure for the Dunion moist-tropical sounding (black) and each of the environmental moisture profiles (gray). (b) Temperature and dewpoint temperature are shown as a function of log-pressure for the Dunion moist-tropical sounding (magenta and green, respectively), along with dewpoint temperature for each of the environmental moisture profiles (gray).

temperature profile, and vary the mixing ratio; this method preserves the temperature while varying the relative humidity. For example, Hill and Lackmann (2009) placed their vortices in a moist envelope where the environmental humidity was held constant within 100 km of the incipient vortex center, linearly reduced between 100 and 150 km, and constant beyond 150-km radius. The environmental moisture reduction factor was applied uniformly in the vertical (i.e., no variations in the vertical were introduced beyond those given in the original sounding). Xu and Wang (2010) also applied a uniform reduction factor in the vertical to create variable initial environments. We adopt a methodology that is motivated by climatological studies demonstrating that tropical moisture variance is maximized near the midtroposphere (e.g., Dunion, 2011; Holloway & Neelin, 2009). Furthermore, relatively high midtropospheric moisture content within tropical waves has been shown to be an important factor contributing to cyclogenesis (Davis & Ahijevych, 2013; Komaromi, 2013).

Beginning with the Dunion moist-tropical sounding (Dunion, 2011), we fix the temperature profile and systematically vary the vertical structure of moisture to produce a set of three soundings. The Dunion moist-tropical sounding is first interpolated to 40-m vertical intervals between the surface and 10-km altitude. This region is smoothed using a 3-km low-pass Lanczos filter with 35 weights. Variations to the smoothed moisture profile are then introduced by applying a Hanning window with a multiplicative factor such that the relative humidity ( $\mathcal{H}$ ) is set to 20%, 40%, or 60% at 4,960-m altitude (~560 hPa; Figure 2a). The dewpoint temperature profiles are reconstructed with these moisture variations and shown on a skew-T log-P diagram in Figure 2b, along with the original Dunion moist-tropical sounding for reference. The  $\mathcal{H} = 60\%$  sounding is nearly identical to the Dunion moist-tropical sounding, and the  $\mathcal{H} = 20\%$

sounding resembles the midlevel moisture content observed during a Saharan air layer event in the North Atlantic basin (Dunion, 2011). We neglect initial horizontal moisture variations aside from those required to satisfy thermal wind balance when superposing an axisymmetric vortex circulation onto a horizontally homogeneous environment. This method is limited in its representation of nature where TCs often develop in asymmetric distributions of moisture; however, we find it fruitful to examine the expansion of TCs in a simplified framework that can be generalized to represent a larger set of environments in future work. The  $\mathcal{H} = 20\%$  and  $\mathcal{H} = 60\%$  environments will henceforth be referred to as dry and moist, respectively.

### 2.3. Numerical Model Setup

Numerical simulations are carried out with the nonhydrostatic, fully compressible Cloud Model 1 (CM1) version 19.7 (Bryan & Fritsch, 2002). As described above, the incipient vortex circulation and environmental moisture are varied to create three different initial conditions for each parameter, resulting in nine experiments. Each of the nine experiments are simulated with the axisymmetric configuration of CM1, and the four experiments representing the small/large incipient vortices and the dry/moist environments are simulated with the full, three-dimensional configuration of CM1. Axisymmetric simulations are computationally inexpensive, and therefore an ensemble of 10 axisymmetric simulations is produced for each of the nine experiments in the original set. The 3-D experimental design is chosen to aid in delineating the underlying processes contributing to TC expansion in three dimensions by selecting the extrema of initial conditions. Following Van Sang et al. (2008), we introduce random moisture perturbations with an amplitude of  $\pm 0.5 \text{ g kg}^{-1}$  to the lowest 500 m of the axisymmetric simulation domains. This method is chosen to examine the sensitivity of TC expansion, and the processes discussed herein, to stochastic processes such as deep, moist convection.

The axisymmetric grid spans 3,050 km in radius and is defined with a uniform 1-km radial grid spacing in the innermost 300 km that gradually stretches to 10-km spacing at the domain boundary. There are 800 radial grid points in total. The vertical grid spans 28 km in altitude and is defined with a grid spacing that stretches from 50 to 500 m in the lowest 5.5 km and is a uniform 500 m above 5.5 km. There are 65 vertical grid points in total, with 12 lying in the lowest 2-km altitude. A Rayleigh damping layer is applied 100 km from the outer horizontal boundary and above 22-km altitude to aid in mitigating the reflection of internal gravity waves.

The 3-D grid spans  $2,040 \text{ km} \times 2,040 \text{ km}$  in the horizontal and is defined with a uniform 2.5-km grid spacing in the innermost 1,200 km that gradually stretches to 11.5-km spacing at the domain boundaries. There are  $600 \times 600$  horizontal grid points in total. The vertical grid and Rayleigh damping layer applied above 22-km altitude are identical to those used in the axisymmetric simulations. We note that the radial grid spacing in the axisymmetric domain is not identical to the horizontal grid spacing in the 3-D domain. The principal findings in this study are not sensitive to the choice of axisymmetric grid spacing (not shown), and therefore we opt to present results from the axisymmetric simulations with a finer 1-km radial grid spacing. Furthermore, we replicated the 3-D simulation of the large TC in the moist environment with a larger horizontal grid spanning  $5,400 \text{ km} \times 5,400 \text{ km}$ ; the expansion rate was nearly identical to the simulation with a relatively smaller grid spanning  $2,040 \text{ km} \times 2,040 \text{ km}$  (not shown), providing confidence that our principal findings are not affected by the horizontal grid size.

Preliminary experimentation with 3-D simulations revealed that TCs developing in quiescent environments absent uniform flow or vertical wind shear did not adequately produce rainbands and outer-core convection that typify TCs observed in nature. Given the aforementioned relationship between convectively driven convergence of absolute angular momentum and TC expansion, we found that 3-D simulations of TCs developing in quiescent environments may not sufficiently represent the salient processes contributing to TC expansion. We found that imposing a uniform flow throughout the 3-D simulation domain facilitates the development of TC rainbands and outer-core convection, thereby producing a more realistic representation of TC structural evolution. The inclusion of a uniform flow throughout the 3-D simulation domain requires periodic boundary conditions in the dimension parallel to the flow; herein, we opt for doubly periodic boundary conditions. TCs developing within periodic domains adapt to their initial environmental conditions and continuously modify their environments.

We gradually impose a  $5 \text{ m s}^{-1}$  uniform westerly flow throughout the domain following a methodology similar to the time-varying point-downscaling (TVPDS) technique (Onderlinde & Nolan, 2017). The uniform flow is introduced by adding a Newtonian relaxation term to the horizontal momentum equations, given by

$$\frac{\partial u}{\partial t} = \dots - \frac{\langle u \rangle - u_{ref}}{\tau_n}, \quad (3)$$

and

$$\frac{\partial v}{\partial t} = \dots - \frac{\langle v \rangle - v_{ref}}{\tau_n}, \quad (4)$$

where  $\langle u \rangle(z)$  and  $\langle v \rangle(z)$  denote the domain-averaged zonal and meridional wind velocities, respectively,  $u_{ref}(z, t)$  and  $v_{ref}(z, t)$  denote the reference zonal and meridional wind profiles to nudge toward, respectively, and  $\tau_n$  is the nudging time scale. Thus, domain-averaged winds at each vertical level are nudged toward a specified reference profile that is a function of height and time, avoiding the introduction of a net circulation into the domain. The nudging time scale  $\tau_n$  controls the rate at which the domain-averaged winds are nudged toward the reference wind profile. We permit each of the vortices to develop deep, moist convection for 24 hr prior to introducing the  $5 \text{ m s}^{-1}$  uniform westerly flow with a 6-hr nudging time scale. A time-varying translational domain is updated each hour in the simulation to track the minimum of a smoothed pressure field that represents the approximate center of each vortex, and the domain translation velocity vector is subtracted from the total wind to produce grid-relative winds. We further refine our specification of the center location with a 2–8-km layer-averaged pressure centroid following the method described by Nguyen et al. (2014).

All simulations are integrated for 8 days on an  $f$  plane corresponding to  $\sim 16^\circ\text{N}$  latitude with underlying sea surface temperatures fixed at  $29^\circ\text{C}$ . Radiative processes are approximated via a simple  $2 \text{ K day}^{-1}$  Newtonian relaxation to the base state temperature profile (Rotunno & Emanuel, 1987). Microphysical processes are parameterized using the Morrison double-moment scheme with graupel selected as the large ice category (Bryan & Morrison, 2012). Subgrid-scale turbulent processes are parameterized using a first-order local closure, commonly referred to as the “Louis PBL scheme” (Bryan et al., 2017; Kepert, 2012; Louis, 1979). The horizontal and vertical eddy viscosities are separately determined given the local flow deformation and the moist Brunt-Väisälä frequency. The heat diffusivity is taken as identical to the momentum diffusivity such that the Prandtl number is unity. This turbulence parameterization requires specifying the horizontal and vertical mixing length scales, chosen herein as  $l_h = 1,000 \text{ m}$  and  $l_v = 100 \text{ m}$ , respectively, for both the axisymmetric and 3-D simulations.

### 3. Results

#### 3.1. Intensity and Initiation of Rapid Intensification

The intensity of each simulated TC is shown as a function of time in Figure 3, where intensity is approximated as the maximum azimuthally averaged wind speed at the lowest model level (25 m). There are no discernible intensity relationships as a function of either incipient vortex circulation or environmental moisture for the axisymmetric ensemble averages, whereas an initially larger incipient vortex circulation or larger environmental moisture generally produces higher-intensity TCs for the 3-D simulations. Discrepancies in the timing to begin rapid intensification (RI) are noted among the axisymmetric ensemble averages and the 3-D simulations. Consistent with previous studies, larger tropospheric moisture content expedites the development phase and initiation of RI as the incipient vortex is more quickly moistened, thereby promoting deep convection (e.g., Kilroy & Smith, 2017; Tao & Zhang, 2014). We define the initiation of RI following a method similar to that used by Judt and Chen (2016) and Rios-Berrios et al. (2018), which is motivated by the approximate 95th percentile of 24-hr overwater TC intensification rates in the North Atlantic basin (Kaplan et al., 2010). The initiation of RI is specified as the first (hourly) time step where the subsequent 24-hr intensification rate exceeds  $15.4 \text{ m s}^{-1}$  and each of the 6-hr intensification rates within the 24-hr time window exceeds  $3.8 \text{ m s}^{-1}$ . Black dots in Figure 3 denote the initiation of RI for each simulation following this definition. To account for timing discrepancies in the initiation of RI and provide a more consistent comparison of

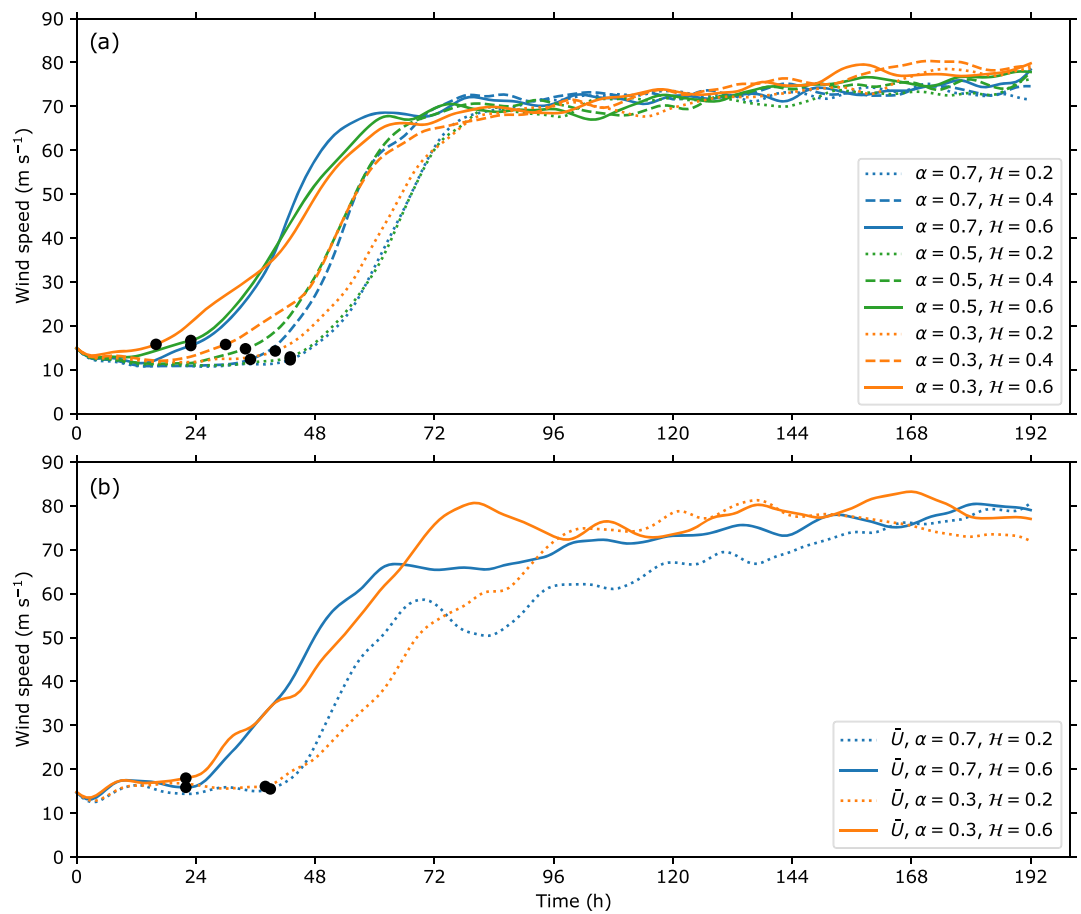


**Figure 3.** The maximum azimuthally averaged wind speed at the lowest model level (25 m) is shown as a function of time for (a) the nine axisymmetric ensemble averages (10 ensemble members each) and (b) the four 3-D simulations. Simulations are distinguished by the modified Rankine vortex decay parameter ( $\alpha$ , color) and by the midlevel environmental relative humidity ( $\mathcal{H}$ , line style).  $\bar{U}$  denotes the presence of a uniform  $5 \text{ m s}^{-1}$  westerly flow for 3-D simulations (see section 2.3 for details). Black dots denote the initiation of rapid intensification for each respective simulation. Each time series is smoothed using a 12-hr low-pass Lanczos filter with nine weights.

TC evolution, we henceforth subtract off the time when RI begins from each simulation when displaying our results. Furthermore, to facilitate the discussion of results as a function of incipient vortex circulation and environmental moisture, we abbreviate references to each simulation as follows: small (*S*), large (*L*), dry (*D*), and moist (*M*). For example, the simulation with a decay parameter of  $\alpha = 0.7$  and midlevel environmental moisture of  $\mathcal{H} = 20\%$  is referred to as the *SD* simulation.

### 3.2. RMW and $R_{gales}$ Evolution

Time series of the azimuthally averaged RMW at the lowest model level and  $R_{gales}$  are shown for all simulations in Figure 4. The shading in Figures 4a and 4b represent 1 standard deviation from the axisymmetric ensemble-mean RMW and  $R_{gales}$ , respectively. In each of the axisymmetric ensemble averages, the RMW contracts to  $\sim 10$ -km radius during the intensification phase and subsequently expands for the remainder of the simulation. 3-D simulations illustrate a similar contraction of the RMW during intensification; however, the RMW does not expand subsequent to the intensification phase for the small TCs. Both sets of axisymmetric and 3-D simulations show that for a given environmental moisture, as the incipient vortex circulation increases, the resulting RMW is larger at all times during the TC life cycle. Furthermore, the axisymmetric ensemble averages show that for a given incipient vortex circulation, TCs embedded in environments with larger moisture content attain a larger RMW; however, this relationship is not present for small TCs in the 3-D simulations.

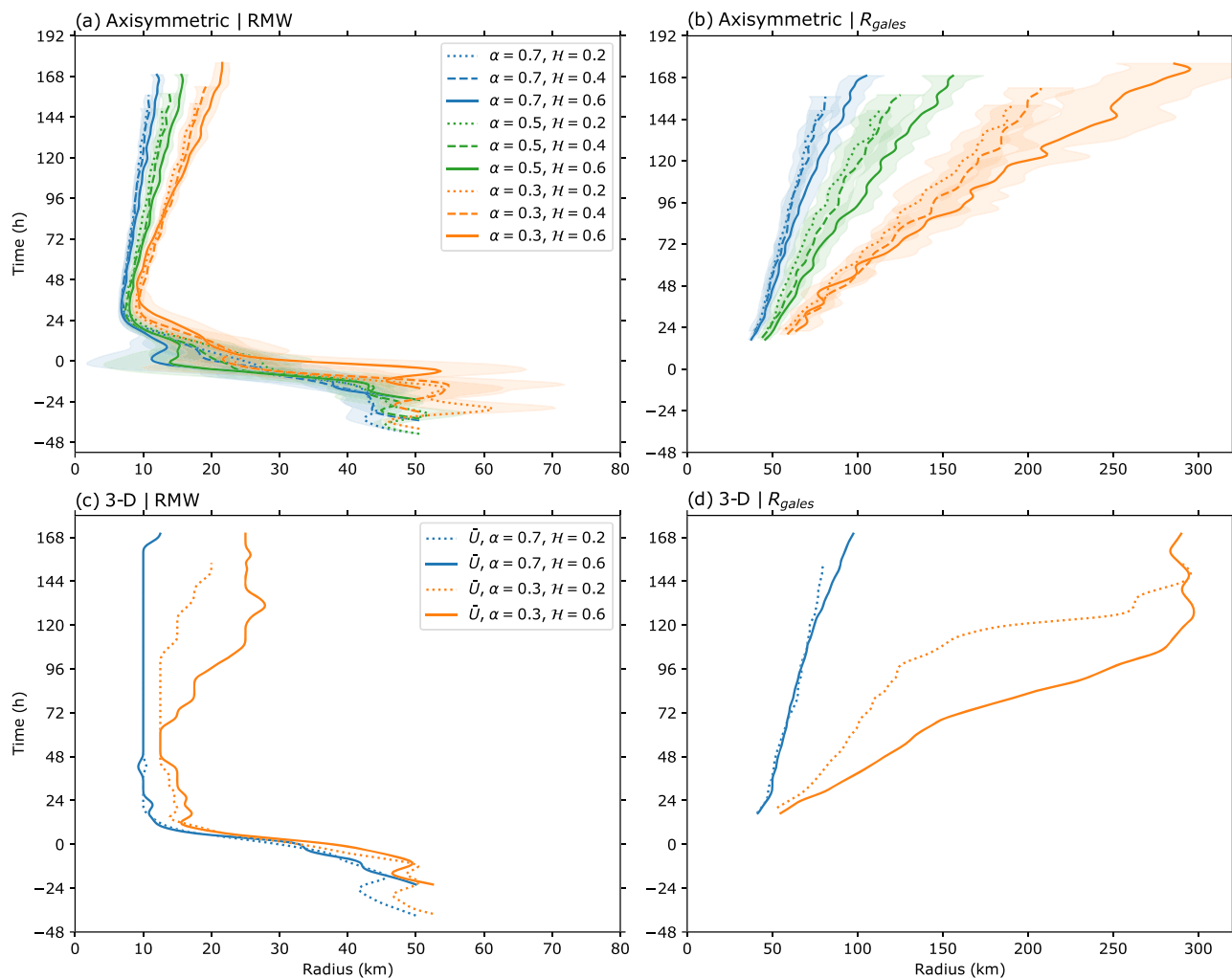


**Figure 4.** The radius of maximum tangential winds (RMW) and the radius of gale-force winds ( $R_{gales}$ ) are shown as a function of time with respect to the initiation of rapid intensification for (a, b) the nine axisymmetric ensemble averages and (c, d) the four 3-D simulations, respectively. Simulations are distinguished by the modified Rankine vortex decay parameter ( $\alpha$ , color) and midlevel environmental relative humidity ( $H$ , line style). The shading represents 1 standard deviation from the axisymmetric ensemble-mean (a) RMW and (b)  $R_{gales}$  for each experiment.  $\bar{U}$  denotes the presence of a uniform  $5 \text{ m s}^{-1}$  westerly flow for 3-D simulations (see section 2.3 for details). Each time series is smoothed using a 12-hr low-pass Lanczos filter with nine weights.

Figure 4 elucidates the principal finding of this study; the incipient vortex circulation places the primary constraint on TC expansion, and in part establishes the expansion rate. An initially large vortex ( $\alpha = 0.3$ ) expands more quickly than its relatively smaller counterpart ( $\alpha = 0.7$ ); therefore, with all other factors contributing to expansion held constant, the contrast in size between the two vortices *increases* with time. Increasing the environmental moisture produces larger TCs when the timing to rapid intensification is left unaccounted; however, a more consistent comparison accounting for the timing to RI reveals that the expansion rate is only slightly modulated by increasing the environmental moisture. The axisymmetric ensemble averages show a slightly quicker expansion rate as the environmental moisture is increased for a given incipient vortex circulation. The degree to which varying the environmental moisture modulates the expansion rate in the 3-D simulations is dependent on the incipient vortex circulation. Increasing the environmental moisture does not influence the expansion rate for initially small vortices, whereas increasing the environmental moisture results in quicker expansion rates for initially large vortices. Furthermore, Figures 4c and 4d show that the expansion rates for the large, 3-D simulations are enhanced when the RMW begins to expand.

To further clarify the relative contributions of incipient vortex circulation and environmental moisture to TC expansion, Figure 5 shows a box plot analysis of  $R_{gales}$  for the axisymmetric ensembles at 48 and 96 hr after

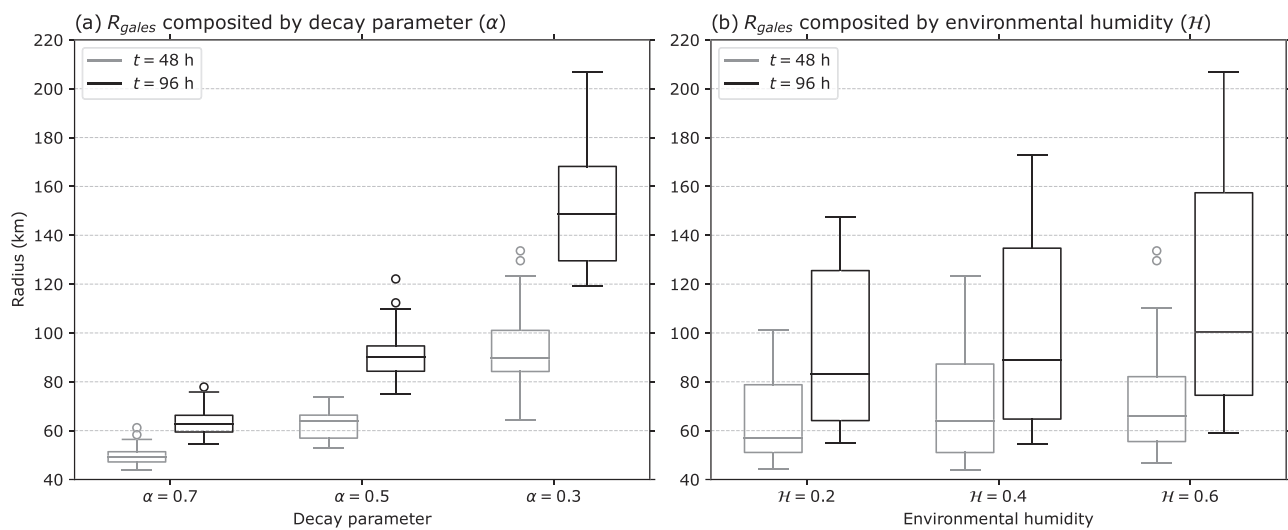


**Figure 5.** Box and whisker plots of the radius of gale force winds ( $R_{gales}$ ) are shown for the axisymmetric ensembles composited by (a) the modified Rankine vortex decay parameter ( $\alpha$ ) and (b) the midlevel environmental relative humidity ( $H$ ). The composited axisymmetric ensemble  $R_{gales}$  distributions are shown in gray at 48 hr after the initiation of rapid intensification (RI) and in black at 96 hr after the initiation of RI. The median  $R_{gales}$  for each composited distribution is given by the horizontal line that dissects each box; the edges of each box represent the lower quartile ( $q_1$ ) and upper quartile ( $q_3$ ) of the composited  $R_{gales}$  distribution; the whiskers extend from  $q_1 - 1.5 \times IQR$  to  $q_3 + 1.5 \times IQR$ , where IQR denotes the interquartile range ( $q_3 - q_1$ ) of the composited distribution; and the circles represent outliers beyond the range of values captured by the whiskers.

the initiation of RI. In general, the variability of  $R_{gales}$  among the axisymmetric ensembles is primarily concentrated along the dimension of incipient vortex circulation, and this is noted by a reduction of the  $R_{gales}$  interquartile range when compositing the axisymmetric ensembles by incipient vortex circulation in contrast to compositing by environmental moisture. Figure 5 further demonstrates that the contrast in the median  $R_{gales}$  between the small and large TCs increases from 48 to 96 hr after the initiation of RI ( $\sim 40$  km difference in the median  $R_{gales}$  to an  $\sim 86$  km difference), whereas the contrast between the dry and moist environments does not vary as much from 48 to 96 hr after the initiation of RI ( $\sim 12$  km difference in the median  $R_{gales}$  to an  $\sim 17$  km difference). To further assess the differences between the axisymmetric ensemble  $R_{gales}$  composited by incipient vortex circulation and environmental moisture, we apply a two-tailed Wilcoxon-Mann-Whitney rank-sum test between each of the composites shown in Figure 5. We construct our hypothesis tests at the 1% significance level (99% confidence) and apply the Šidák correction to control the familywise error rate arising from multiple hypothesis tests; that is, we specify the familywise significance level  $\beta = 0.01$  and apply the Šidák correction for  $n = 12$  hypothesis tests by requiring that each null hypothesis is rejected only when its  $p$  value  $< \beta_S = 1 - (1 - \beta)^{1/n} = 0.000837$  (99.99163% confidence).

The differences between the axisymmetric ensemble  $R_{gales}$  for the small and large TCs are statistically significant at the 1% level ( $p$  value  $< 0.000837$  at both 48 and 96 hr after the initiation of RI). On the contrary, the differences between the axisymmetric ensemble  $R_{gales}$  for the dry and moist environments are not statistically significant at the 1% level ( $p$  value = 0.16 at 48 hr after the initiation of RI;  $p$  value = 0.05 at 96 hr after the initiation of RI). Increasing the environmental moisture promotes expansion, given that the contrast in the median  $R_{gales}$  between the dry and moist environments slightly increases from 48 to 96 hr after the initiation of RI; however, varying the environmental moisture has a relatively minor contribution to the expansion rate in contrast to varying the incipient vortex circulation. Therefore, we have additional evidence to corroborate the statement that within our idealized modeling framework, the incipient vortex circulation places the primary constraint on TC expansion. Henceforth, we will discuss results from the 3-D simulations. Although computational expenses precluded running ensembles for each 3-D experiment, the principal findings highlighted in this section are present in both the axisymmetric ensemble averages and 3-D simulations, providing confidence in the processes discussed herein.

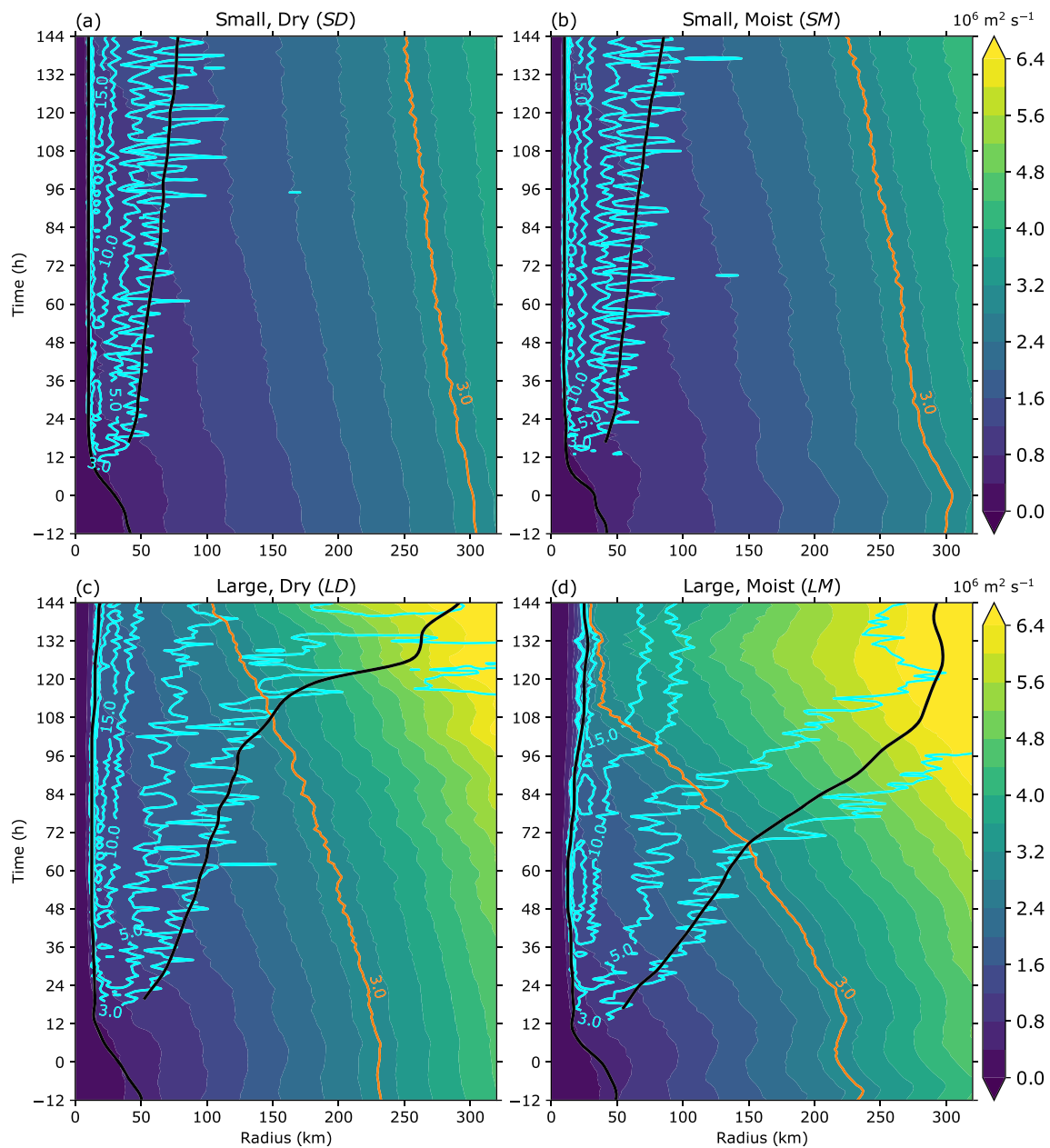


**Figure 6.** Azimuthally averaged absolute angular momentum at 1-km altitude (shaded), 0–1-km altitude layer-averaged radial inflow magnitude (cyan contours at 3, 5, 10, and 15  $\text{m s}^{-1}$ ), and the absolute angular momentum surface corresponding to  $3.0 \times 10^6 \text{ m}^2 \text{ s}^{-1}$  (orange) are shown as a function of time relative to the initiation of rapid intensification for the 3-D simulations: (a) SD, (b) SM, (c) LD, and (d) LM. The innermost black curve in each panel is the radius of maximum tangential winds (RMW) and the outermost black curve is the radius of gale-force winds ( $R_{gales}$ ).

As noted in section 1, TC expansion is inextricably linked to convectively driven convergence of absolute angular momentum toward the TC center of circulation. To illustrate this relationship, Figure 6 shows the azimuthally averaged evolution of absolute angular momentum ( $M$ ) for each TC at 1-km altitude. Overlaid in orange is the  $M$  surface corresponding to  $3.0 \times 10^6 \text{ m}^2 \text{ s}^{-1}$  (for simplicity, the  $M = 3.0$  surface) for each respective TC. The large TCs begin with a greater amount of outer-core  $M$  compared to the small TCs and subsequently converge a substantially greater amount throughout their life cycles. Furthermore, the extent of radial inflow is a function of incipient vortex circulation, such that the small TCs do not have radial inflow exceeding  $3 \text{ m s}^{-1}$  beyond 100-km radius. Collectively, this evolution is captured by the  $M = 3$  .0 surface beginning at  $\sim 300$ -km radius for the small TCs and contracting  $\sim 50$ – $75$  km, whereas the  $M = 3.0$

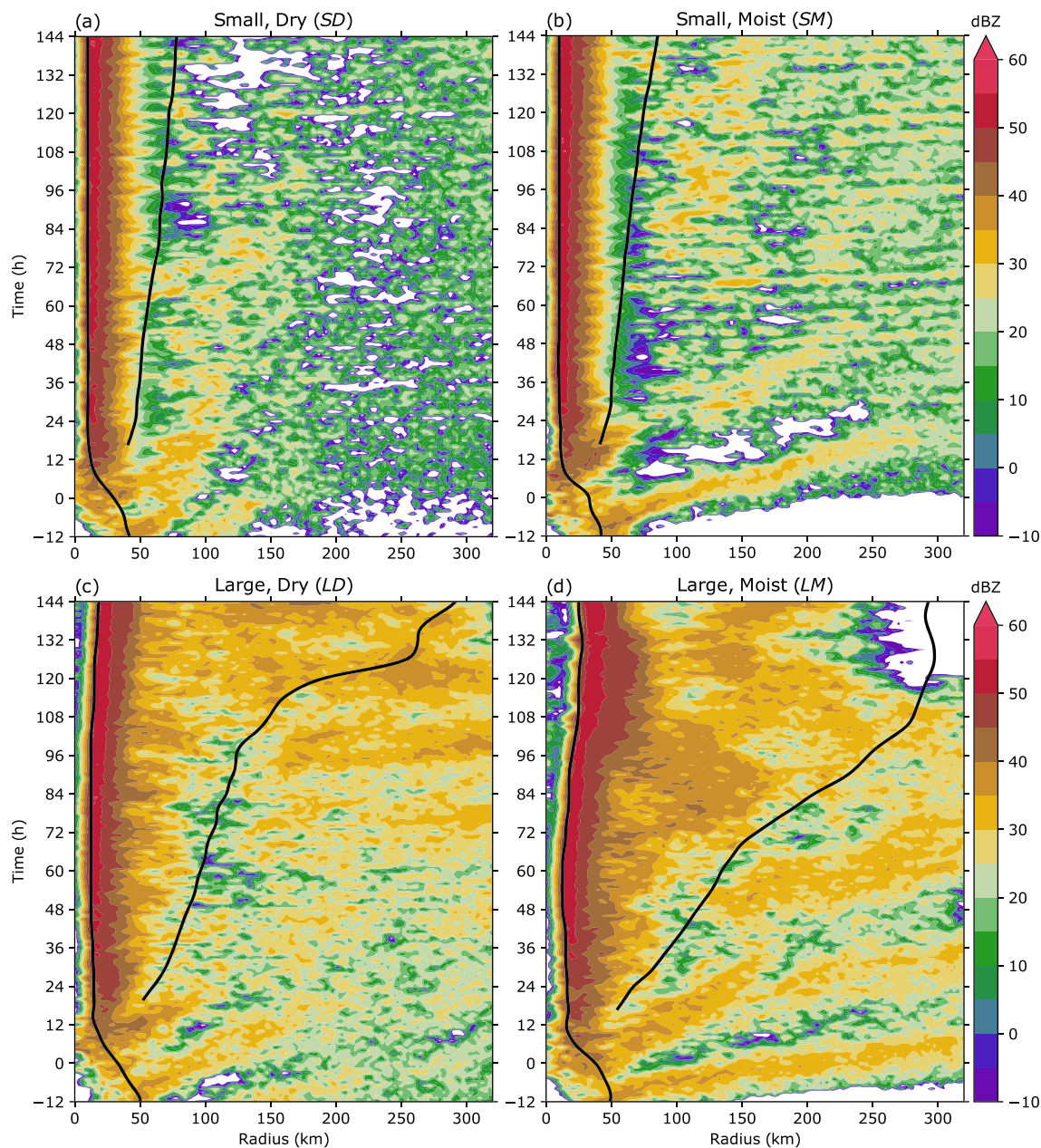


**Figure 7.** Radar reflectivity (dBZ) at 2-km altitude is shown as a function of radius and time relative to the initiation of rapid intensification for the 3-D simulations: (a) SD, (b) SM, (c) LD, and (d) LM. The innermost black curve in each panel is the radius of maximum tangential winds (RMW) and the outermost black curve is the radius of gale-force winds ( $R_{gales}$ ).

surface begins at  $\sim 230$ -km radius for the large TCs and contracts over 200 km; the  $M = 3.0$  surface is eventually subsumed into the inner-core circulation of the LM TC (Figure 6d). A combination of an initially greater amount of outer-core  $M$  and a broader extent of radial inflow contributes to the large TCs converging a substantially greater amount of  $M$  throughout their life cycles compared to the small TCs. The following sections will demonstrate that this finding is primarily related to the areal distribution and nature of convection found in the outer-core region.

### 3.3. Convective Evolution

The evolution of convection for each 3-D simulation is shown by the azimuthally averaged radar reflectivity (dBZ) at 2-km altitude in Figure 7. We choose 2-km altitude to capture the contributions from a bottom-

heavy updraft mass flux profile to lower-tropospheric convergence that draws in absolute angular momentum, thereby providing a direct relationship between convective activity and expansion. The following results remain consistent when analyzing the composite radar reflectivity (not shown). Each simulated TC is characterized by vigorous eyewall convection near the RMW, denoted by reflectivity values exceeding 50 dBZ. Notable differences are found radially outward of the RMW, where decreasing the incipient vortex circulation strength or environmental moisture generally corresponds to weaker azimuthally-averaged convection. Figures 7c and 7d show that the aforementioned expanding RMW in the large TCs is accompanied by radially propagating convection that contributes to an expansion of the eyewall in both simulations. We examined animations of radar reflectivity and potential vorticity (PV) and noted an increase in the amount of spiral rainband convection and a subsequent growth of the eye region during the time period that the RMW expands for the large TCs (not shown). The animations suggest that the eyewall may have expanded via PV mixing near the eye-eyewall interface or an eyewall replacement cycle. We reserve a thorough analysis of the processes contributing to eyewall expansion in the large TCs for future work. In general, the strength of outer-core convection varies monotonically with both the incipient vortex circulation and environmental moisture.

To further investigate how the areal distribution of convection varies with the incipient vortex circulation and environmental moisture, Cartesian snapshots of radar reflectivity at 2-km altitude, 72 hr after the initiation of RI, are shown for each simulation in Figure 8. As the incipient vortex circulation is decreased, outer-core convection is relatively scarce and characterized by small-scale, isolated convective elements. On the contrary, as the incipient vortex circulation is increased, outer-core convection abounds and is characterized by relatively large-scale rainbands and mesoscale convective systems. Increasing the environmental moisture also increases the amount of convection but to a relatively minor extent in comparison to increasing the incipient vortex circulation. Furthermore, increasing the environmental moisture does not have a strong influence on the azimuthal scale of convection.

We quantify how the scale of outer-core convection varies with the incipient vortex circulation and environmental moisture by representing the radar reflectivity at 2-km altitude, given by  $Z(r, j, t)$ , as a Fourier series along the azimuthal dimension

$$Z_m(r, t) = \sum_{j=0}^{J-1} Z(r, j, t) [\cos(2\pi m j / J) + i \sin(2\pi m j / J)], \quad (5)$$

where  $m$  is the azimuthal wave number ( $m = 0, 1, 2, \dots, 180$ ),  $r$  the radius,  $j$  the azimuth angle in degrees ( $j = 0, 1, \dots, 2, \dots, J, = 360$ ), and  $t$  the time. The Fourier coefficient for each azimuthal wave number is given by  $Z_m(r, t)$ . Then, the power spectrum for each azimuthal wave number is given by

$$\mathcal{Z}_m(r, t) = \frac{1}{J^2} |Z_m(r, t)|^2, \quad (6)$$

and the normalized power spectrum for each azimuthal wave number is given by

$$\hat{\mathcal{Z}}_m(r, t) = \frac{\mathcal{Z}_m(r, t)}{\sum_m \mathcal{Z}_m(r, t)}. \quad (7)$$

The normalized power spectrum (7) is computed for reflectivity at 2-km altitude between 100 and 300 km radius and for each hourly time step. Normalized power spectra are then area-averaged between 100 and 300 km radius and cumulatively summed over all wave numbers for each hourly time step.

Figure 9 shows the cumulative normalized power spectra at 48 and 72 hr after the initiation of RI for each simulation. The median cumulative power of outer-core reflectivity occurs between azimuthal wave numbers 4–8 for the large TCs and above azimuthal wave number 9 for the small TCs. Therefore, the median distribution of convection is shifted toward larger scales as the incipient vortex circulation is increased. In general, the large TCs have a propensity to develop relatively large-scale convection in the outer-core region throughout their life cycle, regardless of the environmental moisture. The outer-core convection for the small TCs exhibits a greater scale-dependence on environmental moisture compared to the large TCs, with the moist environment producing larger scales of convection (i.e., smaller azimuthal wave numbers);

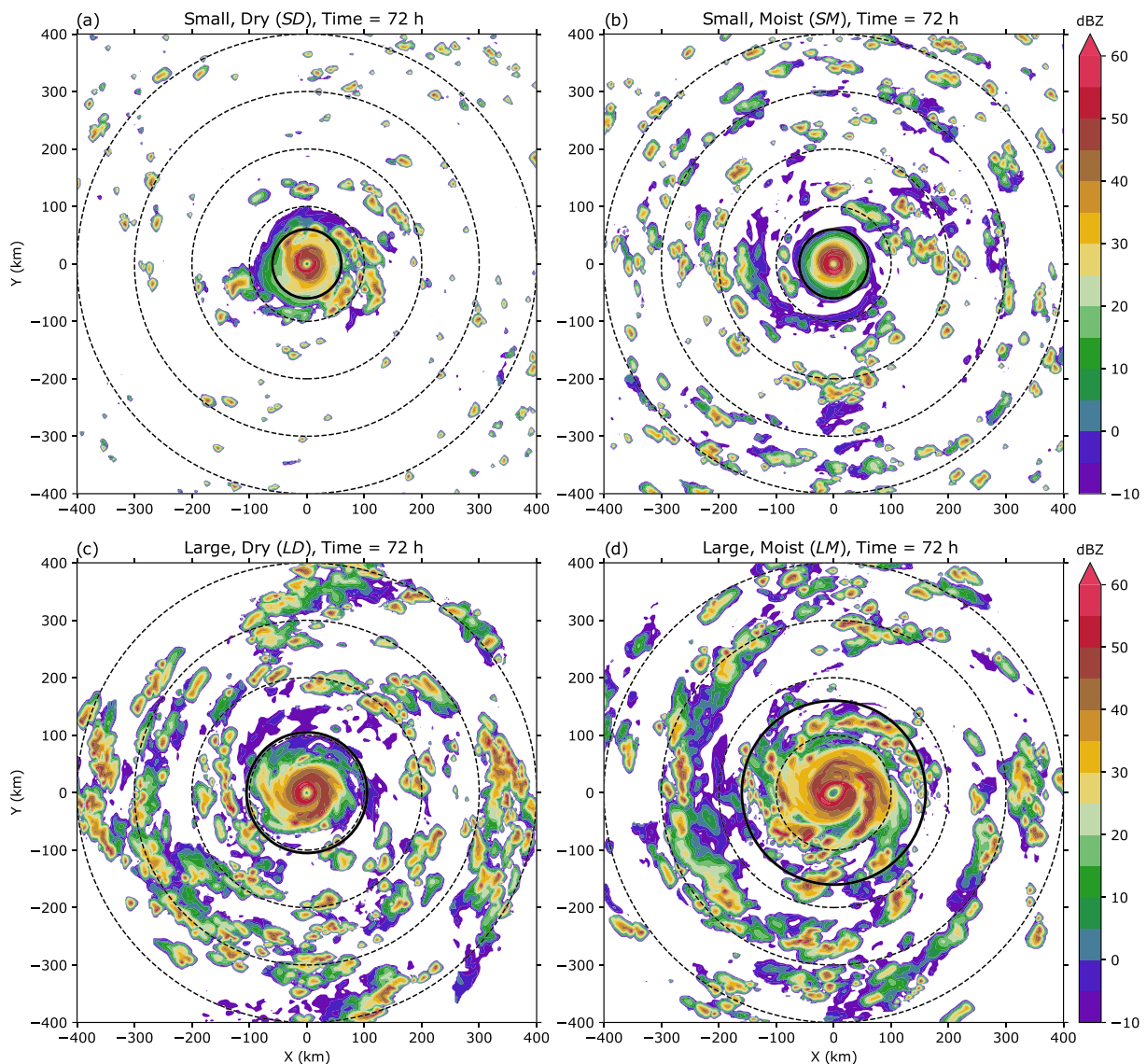


**Figure 8.** Cartesian snapshots of radar reflectivity (dBZ) at 2-km altitude, 72 hr after the initiation of rapid intensification, are shown for the (a) SD, (b) SM, (c) LD, and (d) LM simulations. Radius rings in increments of 100 km from the center of each TC are given by the dashed-black lines, and the radius of gale-force winds ( $R_{gales}$ ) for each respective TC is given by the solid black line.

however, Figure 4d suggests that differences in the scales of outer-core convection between the SD and SM TCs have a relatively negligible influence on the their expansion rates. Although the median cumulative power of outer-core reflectivity for the small TCs shifts to smaller azimuthal wave numbers (i.e., larger scales) when increasing the environmental moisture, the overall distribution of outer-core convection for the small TCs remains best characterized by isolated convective elements (see Figures 8a and 8b). Furthermore, we surmise that the scale and duration of outer-core convection are interdependent, such that relatively small-scale outer-core convection with a short life cycle will converge a lesser amount absolute angular momentum in contrast to large-scale outer-core convection. The following section will further investigate differences in the nature of convection among the simulated TCs to elucidate the differences in expansion rates.

### 3.4. Vertical Mass Flux Distributions

We begin comparing the nature of convection between the simulated TCs via frequency distributions of vertical mass flux within the inner- and outer-core regions. We define the inner-core region as the area enclosed

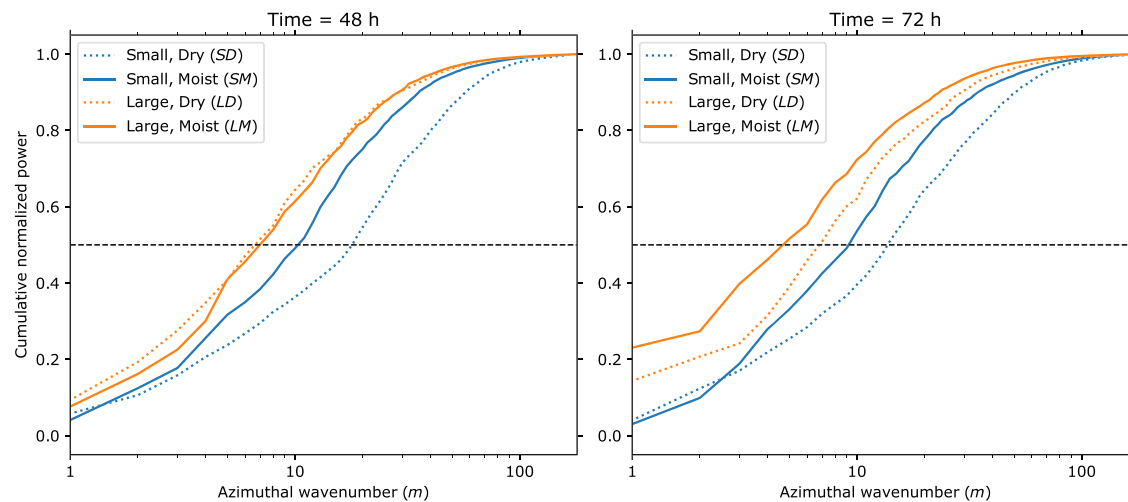


**Figure 9.** Cumulative normalized power spectra of outer-core ( $r = 100\text{--}300$  km) radar reflectivity at 2-km altitude are shown as a function of azimuthal wave number ( $m$ ) for each simulation at (left) 48 hr and (right) 72 hr after the initiation of rapid intensification. The dashed-black line denotes the median cumulative normalized power. See text for additional details on how the cumulative normalized power spectra are constructed.

by  $r \leq 50$  km; this definition is chosen to capture the evolution of convection enclosed by the initial RMW for each TC ( $r = 50$  km), including the eyewall, principal rainbands, and secondary rainbands (Houze, 2010). We define the outer-core region as the area enclosed by  $100 \leq r \leq 300$  km; this definition is chosen to capture the evolution of convection beyond twice the initial RMW for each TC, including principal and secondary rainbands that propagate from the inner- to outer-core region, and distant rainbands (Houze, 2010). We tested several definitions for the inner- and outer-core regions, including dynamic boundaries that follow the RMW (e.g., Hence & Houze, 2012). We elect to use the aforementioned static boundaries when distinguishing between the inner- and outer-core regions to preserve the same number of grid points compared between each TC and to avoid issues with boundaries that account for the RMW given that it flares radially outward at upper levels in the TC circulation. Results remain qualitatively similar when using a definition that accounts for the RMW. Furthermore, we created inner- and outer-core vertical mass flux frequency distributions as a function of altitude for various time windows and found that the results remain largely consistent regardless of the initial window time or its length (not shown). Therefore, we choose to show the vertical mass flux frequency distributions during the 12-hr time window beginning 48-hr after the initiation of RI for each TC. This time window captures the evolution of convection in each TC subsequent to its bulk intensification phase (see Figure 3) and coincides with the previous reflectivity spectral analysis (Figure 9).

Figure 10 shows individual quantiles from the inner-core ( $r \leq 50$  km) vertical mass flux distribution for each TC between 48–60 hr after the initiation of RI. Vertical mass flux quantiles are shown separately for TCs in the dry and moist environments to facilitate comparisons between the small and large TCs. Beginning with the dry environment (Figure 10, top), the LD TC is characterized by a higher frequency of modest-to-strong inner-core updraft mass fluxes throughout the troposphere compared to the SD TC; however, the SD TC has a higher frequency of the strongest inner-core updraft mass fluxes. This result is illustrated by the 75%, 90%, 95%, and 99% updraft mass flux quantiles occurring at stronger magnitudes for the LD TC, but the 99.9% updraft mass flux quantile occurring at stronger magnitudes for the SD TC. Furthermore, the LD TC is characterized by a higher frequency of modest-to-strong inner-core downdraft mass fluxes between  $\sim 4$  and 10 km altitude compared to the SD TC, but the SD TC has a higher frequency of the strongest inner-core downdraft mass fluxes.

Transitioning to the moist environment (Figure 10, bottom), differences between the LM and SM TCs are largely similar to those found among TCs in the dry environment. One noticeable difference is that a higher frequency of the strongest updraft mass fluxes for the SM TC is only found above 8-km altitude rather than throughout the troposphere as in the dry environment. It is also worth noting that differences in the inner-core vertical mass flux distributions between the small and large TCs are more pronounced in the

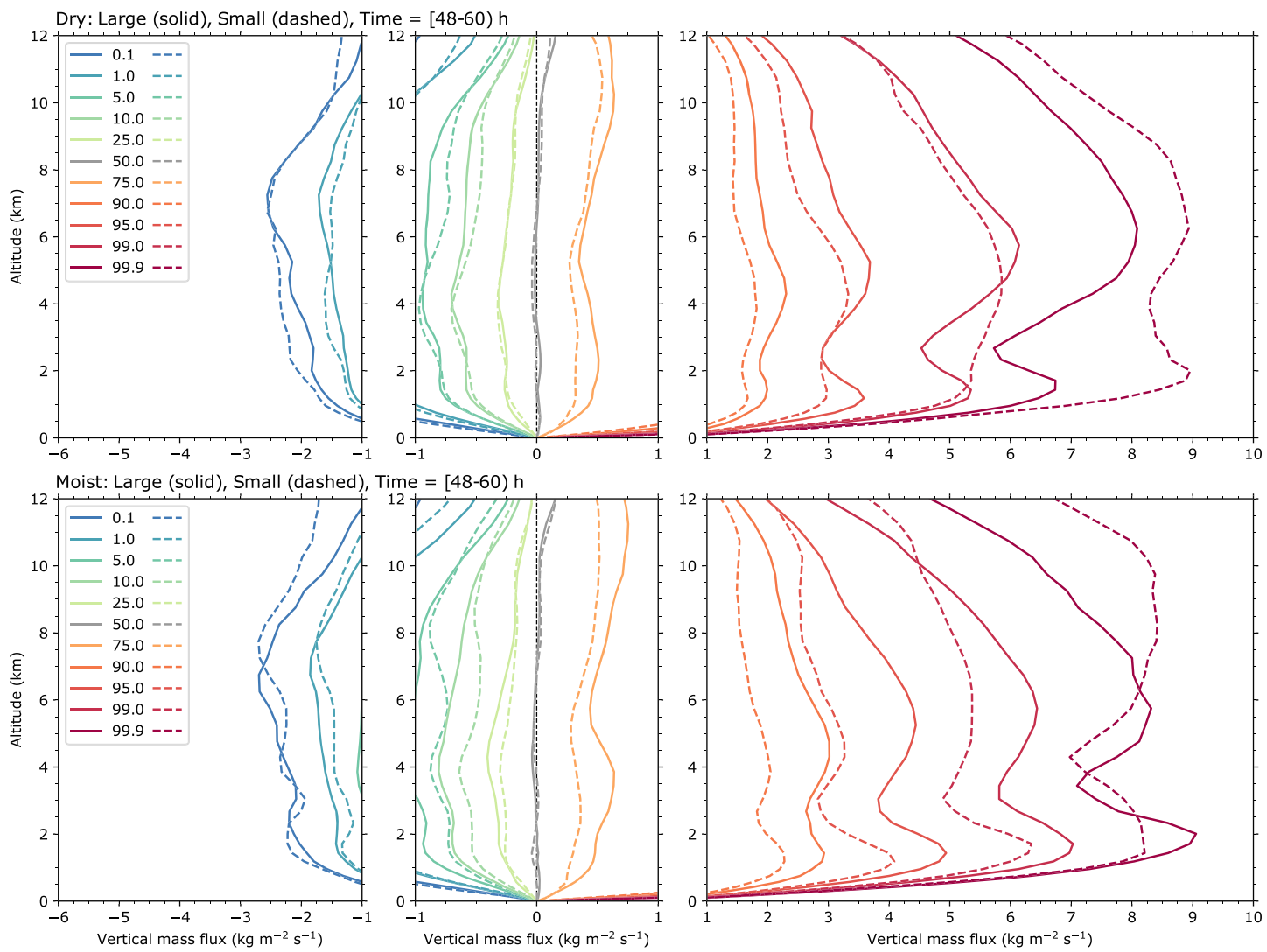


**Figure 10.** Individual quantiles (colors) from the inner-core ( $r \leq 50$  km) vertical mass flux distribution are shown as a function of altitude for each TC between 48–60 hr after the initiation of rapid intensification. (top) Vertical mass flux quantiles are shown for the (solid) large, dry (LD) TC and the (dashed) small, dry (SD) TC. (bottom) Vertical mass flux quantiles are shown for the (solid) large, moist (LM) TC, and the (dashed) small, moist (SM) TC. The middle panels are horizontally stretched to twice the spacing between vertical mass flux values compared to the left and right panels.

moist environment compared to the dry environment. In general, the vertical mass flux distributions shown in Figure 10 demonstrate that subsequent to the bulk intensification phase, an initially large vortex is characterized by a higher frequency of modest-to-strong inner-core vertical mass fluxes compared to its relatively smaller counterpart that is instead characterized by a higher frequency of the strongest inner-core vertical mass fluxes.

Figure 11 shows individual quantiles from the outer-core ( $100 \leq r \leq 300$  km) vertical mass flux distribution for each TC between 48 and 60 hr after the initiation of RI. The general results are consistent when comparing the small and large TCs for both the dry and moist environments; the large TCs are characterized by stronger outer-core updraft and downdraft mass fluxes compared to the small TCs. In contrast to the inner-core vertical mass flux analysis, large TCs exhibit a higher frequency of outer-core updraft and downdraft mass fluxes for all quantiles. A higher frequency of stronger outer-core updraft and downdraft mass fluxes for all quantiles corresponds with the greater amount of outer-core convection previously noted for the large TCs (see Figures 7 and 8). Additionally, stronger magnitudes of vertical mass flux correspond to relatively stronger outer-core convection for the large TCs. Collectively, Figure 11 demonstrates that for a

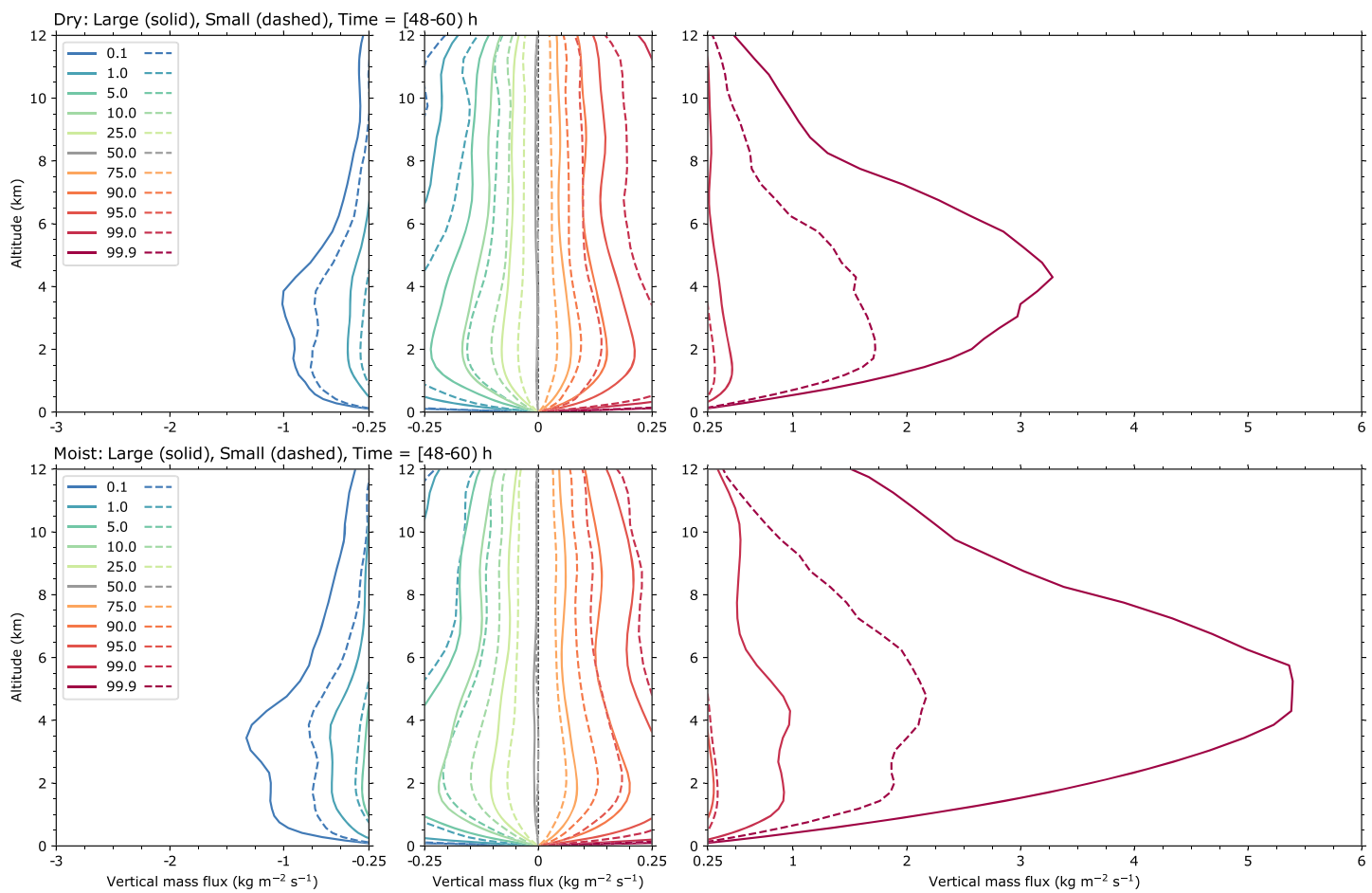


**Figure 11.** As in Figure 9, but for the outer-core ( $100 \leq r \leq 300$  km) vertical mass flux distribution. The middle panels are horizontally stretched to 4 times the spacing between vertical mass flux values compared to the left and right panels.

given environment, the large TCs are distinguished from their relatively smaller counterparts by a greater amount of stronger outer-core convection. The following section will link differences in the nature of outer-core convection discussed in the preceding sections to the variable expansion rates noted for each TC by analyzing the absolute circulation evolution.

### 3.5. Absolute Circulation Evolution

Results discussed up to this point have demonstrated that large TCs are primarily distinguished from their relatively smaller counterparts by more abundant outer-core convection that occurs at a larger scale and transports a greater amount of mass throughout the troposphere. Here we investigate the relationship between the nature of outer-core convection and TC expansion rates via the absolute circulation equation. Following the discussion in section 2 of Davis and Galarneau (2009) and section 1 of Raymond et al. (2011), we formulate the absolute circulation equation in a geometric cylindrical coordinate framework as

$$\frac{\partial C}{\partial t} = -\bar{\eta}_z \tilde{\delta} A - \oint \eta'_z u' dl - \oint w \frac{\partial v}{\partial z} dl + \oint F_t dl, \quad (8)$$

where  $C$  is the absolute circulation,  $t$  the time,  $\eta_z$  the absolute vertical vorticity,  $\tilde{\delta}$  the area-averaged horizontal divergence within the area ( $A$ ) bounded by the integration circuit,  $u$  the radial velocity,  $v$  the tangential velocity,  $w$  the vertical velocity, and  $F_t$  the friction opposing the tangential circulation (i.e., opposing flow along the circuit). In a geometric cylindrical coordinate framework, the integration of terms on the right-hand side of Equation 8 occurs along a circuit of constant radius and altitude in the

counterclockwise direction, where  $dl$  is the incremental length along the circuit path. An overbar denotes the azimuthal mean (i.e., average along the circuit) and primes denote deviations from the azimuthal mean (i.e., asymmetries or eddies).

The terms on the right-hand side of Equation 8 represent contributions from (1) the product of area-integrated horizontal divergence within the circuit and azimuthal-mean absolute vorticity along the circuit, (2) asymmetric fluxes of absolute vertical vorticity across the circuit, (3) the flux of absolute vertical vorticity across the circuit arising from tilting horizontal vorticity normal to the circuit, and (4) the flux of absolute vertical vorticity across the circuit associated with friction that opposes the tangential circulation. For simplicity, we henceforth refer to the contributions as stretching, eddy fluxes, tilting, and friction, respectively. As in Rios-Berrios et al. (2016), Equation 8 is normalized by the area enclosed by the circuit and integrated forward in time from  $t_0$  to  $t_1$ , yielding the area-averaged absolute vorticity change (henceforth, area-averaged vorticity change for simplicity)

$$\begin{aligned}\tilde{\eta}_z(t_1) - \tilde{\eta}_z(t_0) = & - \int_{t_0}^{t_1} \overline{\eta}_z \tilde{\delta} dt - \frac{1}{A} \int_{t_0}^{t_1} \oint \eta'_z u' dl dt \\ & - \frac{1}{A} \int_{t_0}^{t_1} \oint w \frac{\partial v}{\partial z} dl dt + \frac{1}{A} \int_{t_0}^{t_1} \oint F_t dl dt.\end{aligned}\quad (9)$$

We create an ensemble-average analysis centered on the 300-km radius circuit to assess contributions from both the inner- and outer-core convection to the area-averaged vorticity change. The ensemble-average approach is designed to mitigate biases introduced from convective activity concentrated along the circuit (Davis & Galarneau, 2009; Rios-Berrios et al., 2016). To produce an ensemble of circuits, we perturb the radial extent of the circular integration domain  $\pm 12.5$  km. Terms on the right-hand side of Equation 9 are then evaluated along each of the circuits and the ensemble average is defined by the area-weighted contributions from all of the circuits.

We note that the area-averaged vorticity change comprises contributions from vortex intensification, strengthening, and expansion (e.g., Merrill, 1984). In particular, the stretching contributions to the area-averaged vorticity change vary as the product between the area-integrated horizontal divergence within the circuit and the azimuthal-mean absolute vertical vorticity along the circuit. We can infer that variations to the horizontal divergence located near the eyewall will impart variations to the stretching contribution evaluated along the 300-km radius circuit; however, we cannot distinguish the “amount” of stretching contributing to vortex intensification and strengthening from the “amount” of stretching contributing to vortex expansion. Therefore, we choose to analyze the area-averaged vorticity change integrated for the 48-hr time window beginning 48 hr after the initiation of RI. The bulk intensification has completed for each TC 48 hr after the initiation of RI (Figure 3) such that the area-averaged vorticity change is primarily comprised of contributions associated with vortex strengthening and expansion. Additionally, the 48-hr integration time window captures the evolution of each TC during the time periods shown in the reflectivity spectral analysis (Figure 9) and the vertical mass flux analyses (Figures 10 and 11).

Ensemble-averaged terms on the right-hand side of Equation 9 are integrated for the 48-hr time window using hourly model output. The sum of terms on the right-hand side of Equation 9 is compared to the net area-averaged vorticity change over the 48-hr integration time window on the left-hand side. We note that hourly model output reasonably captures the quantitative area-averaged vorticity change for each TC (Figure 12), providing confidence in the assessment of individual terms in the budget and comparisons between the TCs. We examined all 48-hr integration time windows beginning 24-hr after the initiation of RI and found that the principal results remain largely consistent (not shown). Toward the later integration time windows for the large TCs, the magnitude of the stretching contributions to the area-averaged vorticity change begins to decrease rapidly as the TCs stop expanding (see Figures 4d and 6d). We have not thoroughly examined the processes contributing to the cessation of expansion for the large TCs and therefore reserve our analyses to the periods of expansion.

Figure 13 shows the individual contributions on the right-hand side of Equation 9 to the area-averaged vorticity change. In general, as the incipient vortex circulation or environmental moisture increases, the stretching contribution to the net area-averaged vorticity change increases. Contributions from stretching

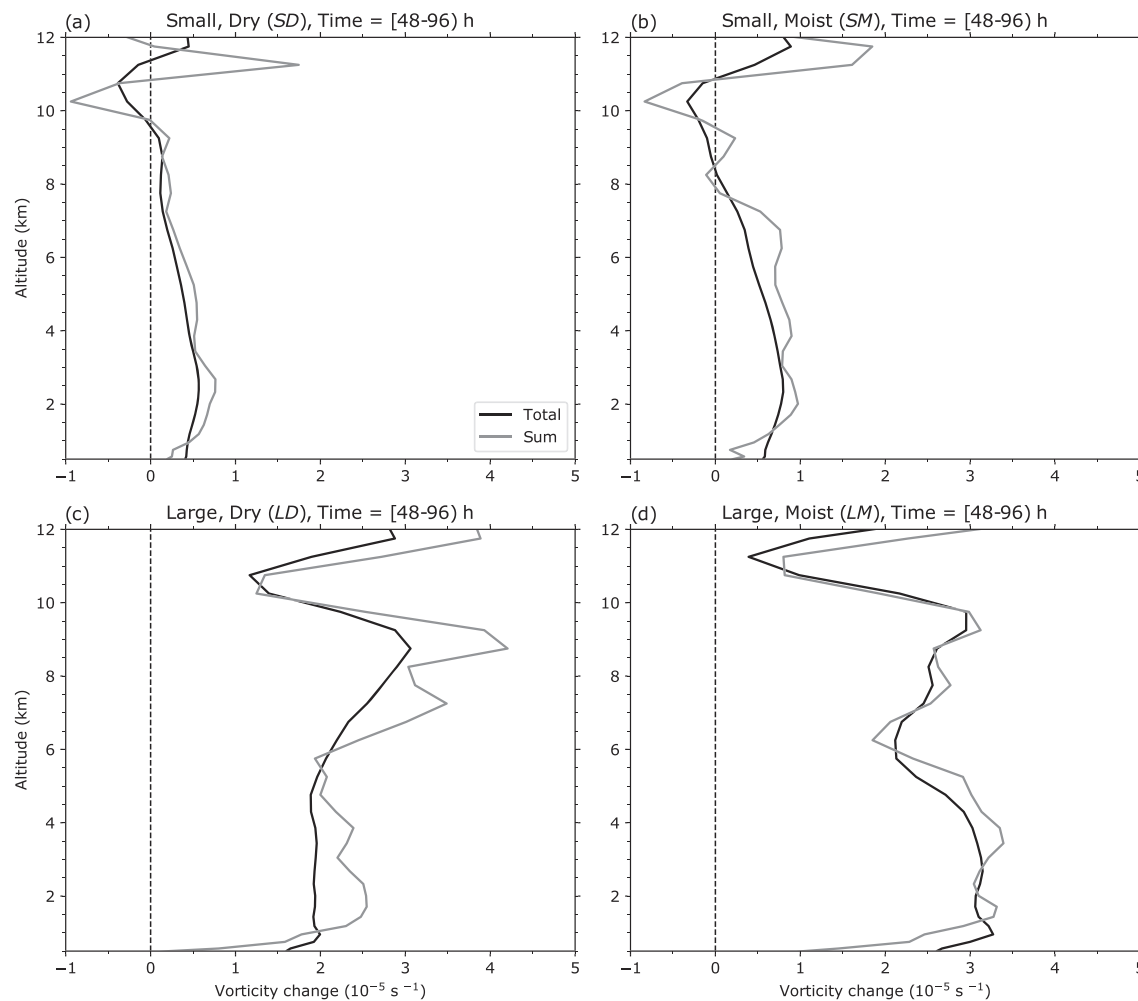


**Figure 12.** The net area-averaged vorticity change [left-hand side of Equation 9] over a 48-hr time window beginning 48 hr after the initiation of RI is shown as a function of altitude in black for the (a) SD, (b) SM, (c) LD, and (d) LM TCs. The sum of individual contributions to the net area-averaged vorticity change [right-hand side of Equation 9] is shown for each respective TC in gray. See text for additional details on the analysis method.

substantiate the statement made earlier that varying the environmental moisture has a stronger influence on expansion rates for the large TCs. When comparing the small TCs, increasing the environmental moisture produces a slight increase in the stretching contributions from the boundary layer through 9-km altitude. In contrast, when comparing the large TCs, increasing the environmental moisture results in approximately twice the stretching contributions from the boundary layer through 9-km altitude. For a given environmental moisture, the large TCs are characterized by a relative abundance of outer-core convection that occurs at a larger scale compared to their relatively smaller counterparts (see Figures 8 and 9), resulting in  $\sim 2\text{--}4$  times more stretching from the boundary layer through 9-km altitude.

As the incipient vortex circulation increases, the tilting contribution to the net area-averaged vorticity change also increases. Differences in tilting primarily arise from differences in the amount of convection located near the 300-km radius circuit; large TCs have a greater amount of outer-core convection and therefore larger tilting contributions to the net area-averaged vorticity change. Differences in tilting are smaller between TCs in the moist environment compared to TCs in the dry environment. When comparing the SM and LM TCs, the SM TC is characterized by less outer-core convection compared to the LM TC, but differences in the amount of convection are not as large compared to those between the SD and LD TCs (e.g., see Figure 8). Additionally, differences in the scale of outer-core convection between the SM and LM TCs are smaller than those between the SD and LD TCs (Figure 9). Therefore, the tilting contribution is  $\sim 2\text{--}3$  times

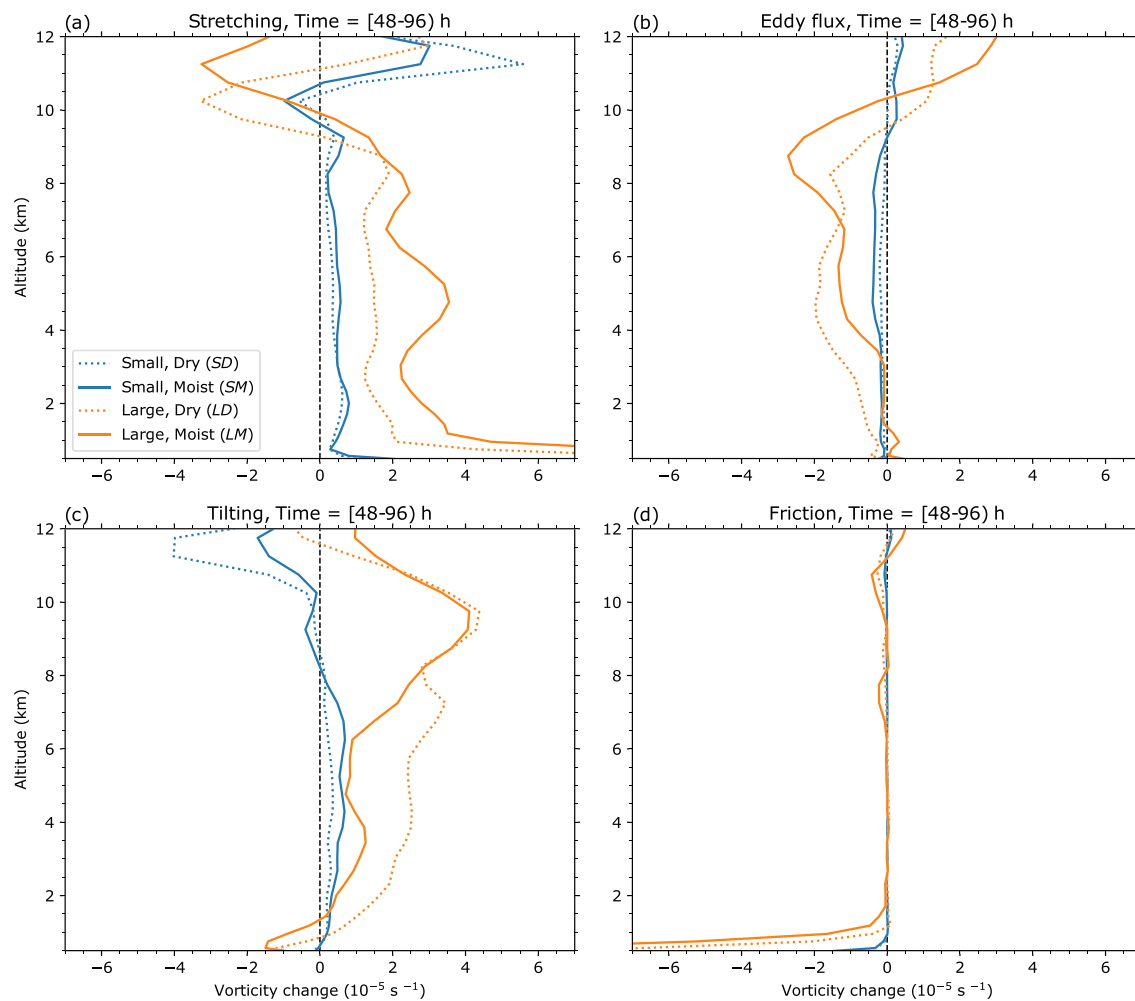


**Figure 13.** The (a) stretching, (b) eddy flux, (c) tilting, and (d) friction contributions to the area-averaged vorticity change [right-hand side of Equation 9] are shown as a function of altitude for each TC, distinguished by incipient vortex circulation (color) and midlevel environmental humidity (line style). See text for additional details on the analysis method.

larger for the *LM* TC compared to the *SM* TC, and  $\sim$ 2–4 times larger for the *LD* TC compared to the *SD* TC. The differences in tilting contributions to the net area-averaged vorticity change between the large and small TCs are generally larger in the middle-to-upper troposphere compared to the lower troposphere. Figure 11 demonstrates that the large TCs have stronger outer-core updraft mass fluxes at all vertical levels throughout the troposphere compared to the small TCs. Given that the large TCs are characterized by initially stronger horizontal vorticity compared to the small TCs, a combination of stronger upper-level updraft mass flux that tilts stronger horizontal vorticity into the vertical results in a larger upper-level tilting contribution.

In general, the eddy vorticity fluxes provide a negative contribution to the net area-averaged vorticity change throughout a deep layer of the troposphere. Negative contributions from eddy vorticity fluxes indicate that cyclonic eddy vorticity produced by outer-core convection is exported across the circuit, or equivalently, that anticyclonic eddy vorticity is imported across the circuit. Differences in the eddy vorticity fluxes between TCs are relatively small below  $\sim$ 4-km altitude and primarily increase with increasing incipient vortex circulation above 4-km altitude, with large TCs exhibiting a greater (negative) eddy vorticity flux compared to the small TCs. Similar to the differences noted in the tilting contributions between the large and small TCs, stronger upper-level updraft mass fluxes for the large TCs produce a greater amount of eddy vorticity that can be transported across the circuit; hence, the differences in eddy vorticity flux contributions between

the large and small TCs are larger in the middle-to-upper troposphere compared to the lower troposphere. Finally, larger TCs are characterized by a stronger outer-core tangential circulation compared to the small TCs, and therefore possess a slightly greater (negative) contribution from the friction term in the boundary layer.

#### 4. Discussion

As discussed in section 1, several past studies have employed similar idealized numerical simulation frameworks to investigate the processes contributing to TC expansion. Hill and Lackmann (2009) posited two potential feedback mechanisms associated with increasing the environmental moisture and producing larger TC expansion rates. Their second feedback mechanism is pertinent to the discussion of results presented herein and therefore we recapitulate the mechanism below. Increasing the environmental moisture of TCs promotes a greater amount of PV generated by radially outward propagating spiral rainbands. PV generated by the spiral rainbands is subsumed by the inner-core PV tower, resulting in a broader PV distribution, and the cyclonic wind field expands in balance with the broader inner-core PV tower. As the cyclonic wind field expands, subsequent heating in spiral rainbands will generate a larger amount of PV given that the diabatic PV tendency is proportional to the magnitude of the absolute vorticity vector. Therefore, an expanding cyclonic wind field promotes a larger amount of PV generation via outward propagating spiral rainbands, which in turn promote an expanding cyclonic wind field; hence, a positive feedback emerges. Although Hill and Lackmann posited this feedback mechanism in association with increasing the environmental moisture, the fundamental processes underlying its premise appear in previous studies that vary the incipient vortex circulation while fixing the environmental moisture (Chan & Chan, 2015; Kilroy & Smith, 2017; Xu & Wang, 2010). Each of these studies emphasize to a varying degree the areal distribution of diabatic heating, the magnitude of the absolute vorticity vector, and their combined influence on TC expansion rates. The findings reported herein are predicated on the same fundamental processes, and thus to a large extent are congruous with the aforementioned studies.

In addition to reproducing findings reported in the aforementioned studies with an independent modeling framework, we further demonstrate that varying the incipient vortex circulation is associated with a scale-dependent response of outer-core convection. Specifically, as the incipient vortex circulation increases, the azimuthal scale of outer-core convection increases. There may be several processes contributing to the noted differences in the scale of outer-core convection as a function of incipient vortex circulation that warrant further investigation. We formulated two related hypotheses to investigate the relationship between the incipient vortex circulation and the upscale growth of outer-core convection. The first hypothesis was formulated from the premise that the small TCs possess dynamically unfavorable outer-core conditions that inhibit convection from growing upscale. To test the first hypothesis, we calculated the filamentation time (Rozoff et al., 2006) and Okubo-Weiss parameter (Dunkerton et al., 2009; Raymond et al., 2011) for the outer-core region with mass-weighted layer averages over three different vertical layers (1–3, 3–5, and 5–8 km). The second hypothesis reversed the perspective from the first hypothesis and was formulated from the premise that the large TCs possess dynamically favorable outer-core conditions that facilitate convection growing upscale. To test the second hypothesis, we calculated the mass-weighted helicity in the outer-core region and the updraft helicity as a function of altitude. The results from both tests were largely inconclusive and did not provide evidence to confirm either of the hypotheses formulated above. We were also unable to reject our hypotheses because exhaustively investigating the relationship between the incipient vortex circulation and the upscale growth of outer-core convection was beyond the scope of our study.

It remains unclear if there is a direct relationship between the amount of straining and the inhibition of upscale growth, or alternatively the degree of helical flow and the facilitation of upscale growth. Therefore, we direct future work toward elucidating the relationship between the incipient vortex circulation and the upscale growth of outer-core convection. We surmise that the scale and duration of outer-core convection are interdependent; thus, their combined influence may in part account for the variable expansion rates noted herein. That is, we expect relatively large-scale convection with a long duration to have a stronger influence on the net area-averaged vorticity change, and hence expansion rate, compared to relatively small-scale convection with a short duration. Detecting and tracking individual convective

elements and quantifying their characteristics can provide a fruitful avenue to begin exploring the propensity for large TCs to develop relatively large-scale outer-core convection (e.g., Terwey & Rozoff, 2014).

Increasing the midlevel environmental moisture initially stimulates the development of outer-core convection; alternatively, decreasing the midlevel environmental moisture initially hinders the development of outer-core convection. TCs developing in the moist environment benefit from initially favorable outer-core conditions whereas TCs developing in the dry environment must gradually overcome a relatively adverse midlevel moisture deficit through convective processes that cumulatively moisten the outer-core region. It is worth noting that the relatively detrimental influences of an initially dry environment discussed above are exacerbated in studies that apply a uniform moisture reduction factor throughout the troposphere. In such studies, surface moisture fluxes must first gradually overcome a relatively dry boundary layer prior to convection developing in the outer-core region; convection in the outer-core region must subsequently overcome a relatively adverse midlevel moisture deficit, thereby prolonging the period of time absent deep, moist convection that is vital to spinning up the outer-core circulation.

We demonstrate that increasing the environmental moisture for large TCs produces a relatively larger contribution to their expansion rates compared to small TCs. Increasing the environmental moisture generally produces a greater amount of outer-core convection that occurs at a slightly larger scale. In both dry and moist environments, the overall distribution of outer-core convection for the small TCs is best characterized by isolated convective elements, whereas the overall distribution of outer-core convection for the large TCs is best characterized by spiral rainbands and mesoscale convective systems. The general morphology of outer-core convection is not categorically modified by increasing the environmental moisture. Therefore, we posit that the sensitivity of the expansion rate to the scale of outer-core convection increases as the median distribution of convection shifts toward larger scales. That is, increasing the azimuthal scale of relatively small-scale outer-core convection produces a negligible contribution to increasing the expansion rate in contrast to increasing the azimuthal scale of relatively large-scale outer-core convection. Collectively, increasing both the incipient vortex circulation and environmental moisture produces a nonlinear increase in TC expansion rates.

Previous studies have demonstrated that TCs possess a sort of “memory” with respect to their incipient circulation (Knaff et al., 2014; Rotunno & Emanuel, 1987), which underlies the statement that large TCs stay large and small TCs stay small. Synthesizing the results presented herein, we further demonstrated that a cumulatively greater amount of absolute angular momentum convergence over time permits an initially large vortex to expand more quickly than its relatively smaller counterpart. Thus, memory of the incipient vortex circulation is imparted upon TC size through variable expansion rates. Schenkel, Lin, Chavas, Vecchi, Oppenheimer, et al. (2018) demonstrated that this memory is largely preserved prior to TCs attaining their lifetime maximum size, but it is attenuated afterward as TCs begin contracting. Therefore, the principal findings reported herein may only be valid prior to TCs attaining their lifetime maximum size. Schenkel, Lin, Chavas, Vecchi, Oppenheimer, et al. (2018) further demonstrated that TCs in the western North Pacific basin experience larger expansion rates compared to TCs in the North Atlantic basin (their Figure 6). Given that TCs developing in the western North Pacific are on average larger than their North Atlantic counterparts, we hypothesize that the results presented by Schenkel, Lin, Chavas, Vecchi, Oppenheimer, et al. (2018) provide evidence to support our principal finding that an initially larger vortex can expand more quickly than its relatively smaller counterpart; however, western North Pacific TCs also develop in environments characterized by larger moisture content and higher sea surface temperatures compared to North Atlantic hurricanes (e.g., Dai, 2006; Gray, 1968), obscuring statements regarding a direct connection or attribution of either variable in isolation. Additionally, the incipient vortex circulation and environmental moisture are interdependent in nature, further obscuring statements regarding the contributions of either variable in isolation. Therefore, the extent to which our principal finding is manifested within the results presented by Schenkel, Lin, Chavas, Vecchi, Oppenheimer, et al. (2018) cannot be estimated, but the parallel between our two studies warrants further investigation.

Our idealized numerical simulations contain simplifying assumptions that may limit the extent to which our results are found in nature. For example, we begin with an axisymmetric incipient vortex circulation and horizontally homogeneous environmental conditions, but precursor disturbances are intrinsically asymmetric and embedded within spatially inhomogeneous environments (e.g., Chang et al., 2017;

McTaggart-Cowan et al., 2008, 2013). Our analysis is limited by excluding contributions from cloud radiative forcing which have been shown to aid the expansion of TC wind fields by producing weak, sustained ascent in the outer-core region that promotes and enhances convective activity (Bu et al., 2014; Fovell et al., 2016). Furthermore, our analysis is limited by imposing a uniform flow throughout the simulation domain instead of introducing vertical shear flow. Previous studies have demonstrated that a low-level flow vector oriented along the upshear-right quadrant of a TC embedded in vertical shear flow favors larger expansion rates (Chen et al., 2018, 2019). Future work will expand upon the results presented in our study by incorporating the aforementioned considerations into experiments with additional numerical simulations and by comparing the idealized numerical simulations to analyses that combine reanalysis products and satellite observations.

## 5. Conclusions

We have investigated the contributions of incipient vortex circulation and environmental moisture to tropical cyclone (TC) expansion with a set of idealized numerical simulations. The incipient vortex circulation strength is varied by fixing the radius of maximum tangential winds (RMW) and modifying the decay of tangential velocity radially outward of the RMW in accordance with observations of North Atlantic basin TCs (Mallen et al., 2005). The environmental moisture is varied by imposing a vertical decay function that largely preserves moisture content within the boundary layer (below  $\sim 850$  hPa) and maximizes the midlevel moisture variance, in accordance with climatological observations of tropical environments (Dunion, 2011; Holloway & Neelin, 2009) and observations of tropical wave disturbances preceding cyclogenesis (Davis & Ahijevych, 2013; Komaromi, 2013).

We find that the azimuthally averaged strength of convection varies monotonically with the incipient vortex circulation. Additionally, large TCs are characterized by radially propagating convection that contributes to an expanding eyewall and further enhances the outer-core expansion rate. We also demonstrate that large TCs exhibit a higher frequency of stronger outer-core updraft and downdraft mass fluxes; that is, the full distribution of outer-core mass fluxes is shifted toward relatively stronger magnitudes as the incipient vortex circulation increases. In assessing the time-integrated absolute circulation evolution, we find that the aggregate influence of increasing the azimuthal scale, amount, and strength of outer-core convection, associated with increasing the incipient vortex circulation, results in approximately 2–4 times larger stretching and tilting contributions. Large TCs are distinguished from their relatively smaller counterparts by a relative abundance of outer-core convection occurring at a larger scale that cumulatively spins up the outer-core TC circulation at a quicker rate via combined stretching and tilting; therefore, with all other factors contributing to expansion held constant, the contrast in size between the two TCs will *increase* with time.

Increasing the midlevel environmental moisture further promotes convection, thereby modulating the expansion rate; however, in the absence of additional factors contributing to expansion other than the incipient vortex circulation, varying the environmental moisture mostly acts to delay or expedite the intensification process in our idealized modeling setup. Therefore, our findings emphasize the importance of accounting for the stage in a TC's life cycle when comparing either the sizes or expansion rates of TCs (e.g., Knaff et al., 2014; Schenkel, Lin, Chavas, Vecchi, Oppenheimer, et al., 2018). We find that the expansion rates of TCs have an asymmetric response to increasing the midlevel environmental moisture; as the incipient vortex circulation increases, variations to the midlevel environmental moisture have more pronounced contributions to the expansion rate. The sensitivity of the expansion rate is primarily related to the azimuthal scale of outer-core convection, and we demonstrate that varying the incipient vortex circulation has a stronger influence on the azimuthal scale of outer-core convection in contrast to varying the mid-level environmental moisture.

Results gathered from our study can aid the development of statistical-dynamical wind radii forecasts (e.g., Knaff et al., 2017). Furthermore, our results may have implications for understanding how the TC size distribution might shift amidst Earth's warming climate system. Dynamical downscaling projections of TC activity have demonstrated that TC size distributions will shift toward larger TCs in a future, warmer climate among all ocean basins except the western North Pacific (Knutson et al., 2015). Schenkel, Lin, Chavas, Vecchi, Knutson, et al. (2018) found that the global TC size distribution will shift toward larger TCs in a future, warmer climate, but that TC size at the time of genesis remains unchanged. Our study motivates

additional investigations into how the wind structure of precursor disturbances might vary in a future, warmer climate and associated implications for TC expansion rates among individual ocean basins.

## Data Availability Statement

The model namelists and environmental soundings required to reproduce the simulations analyzed herein can be accessed via the Zenodo repository located at <https://zenodo.org/record/3891990>.

## Acknowledgments

This work was funded by the Office of Naval Research Awards N000141613033 and N000142012069 and the National Science Foundation (NSF) Award AGS-1701225. J. M. was also supported by the NSF Bridge to the Doctorate Fellowship Award 004863-00003. We thank George Bryan for providing the code to implement time varying point downscaling in CM1. We thank three anonymous reviewers for their insightful comments that have improved the overall quality of our manuscript.

## References

- Arakawa, H. (1952). Mame-Taifu or midget typhoon (small storms of typhoon intensity). *Geophysical Magazine*, 24, 463–474.
- Brand, S. (1972). Very large and very small typhoons of the western North Pacific Ocean. *Journal of the Meteorological Society of Japan*, 50, 332–341.
- Bryan, G. H., & Fritsch, J. M. (2002). A benchmark simulation for moist nonhydrostatic numerical models. *Monthly Weather Review*, 130, 2917–2928. [https://doi.org/10.1175/1520-0493\(2002\)130<2917:ABSFMN>2.0.CO;2](https://doi.org/10.1175/1520-0493(2002)130<2917:ABSFMN>2.0.CO;2)
- Bryan, G. H., & Morrison, H. (2012). Sensitivity of a simulated squall line to horizontal resolution and parameterization of microphysics. *Monthly Weather Review*, 140, 202–225. <https://doi.org/10.1175/MWR-D-11-00046.1>
- Bryan, H. G., Worsnop, R. P., Lundquist, J. K., & Zhang, J. A. (2017). A simple method for simulating wind profiles in the boundary layer of tropical cyclones. *Boundary-Layer Meteorology*, 162, 475–502. <https://doi.org/10.1007/s10546-016-0207-0>
- Bu, Y. P., Fovell, R. G., & Corbosiero, K. L. (2014). Influence of cloud-radiative forcing on tropical cyclone structure. *Journal of the Atmospheric Sciences*, 71, 1644–1662. <https://doi.org/10.1175/JAS-D-13-0265.1>
- Carrasco, C. A., Landsea, C. W., & Lin, Y.-H. (2014). The influence of tropical cyclone size on its intensification. *Weather and Forecasting*, 29, 582–590. <https://doi.org/10.1175/WAF-D-13-00092.1>
- Chan, K. T. F., & Chan, J. C. L. (2012). Size and strength of tropical cyclones as inferred from QuikSCAT data. *Monthly Weather Review*, 140, 811–824. <https://doi.org/10.1175/MWR-D-10-05062.1>
- Chan, K. T. F., & Chan, J. C. L. (2014). Impacts of initial vortex size and planetary vorticity on tropical cyclone size. *Quarterly Journal of the Royal Meteorological Society*, 140, 2235–2248. <https://doi.org/10.1002/qj.2292>
- Chan, K. T. F., & Chan, J. C. L. (2015). Impacts of vortex intensity and outer winds on tropical cyclone size. *Quarterly Journal of the Royal Meteorological Society*, 141, 525–537. <https://doi.org/10.1002/qj.2374>
- Chang, M., Ho, C.-H., Park, M.-S., Kim, J., & Ahn, M.-H. (2017). Multiday evolution of convective bursts during western North Pacific tropical cyclone development and nondevelopment using geostationary satellite measurements. *Journal of Geophysical Research: Atmospheres*, 122, 1635–1649. <https://doi.org/10.1002/2016JD025535>
- Chavas, D. R., & Emanuel, K. A. (2010). A QuickSCAT climatology of tropical cyclone size. *Geophysical Research Letters*, 37, L18816. <https://doi.org/10.1029/2010GL044558>
- Chen, B.-F., Davis, C. A., & Kuo, Y.-H. (2018). Effects of low-level flow orientation and vertical shear on the structure and intensity of tropical cyclones. *Monthly Weather Review*, 146, 2447–2467. <https://doi.org/10.1175/MWR-D-17-0379.1>
- Chen, B.-F., Davis, C. A., & Kuo, Y.-H. (2019). An idealized numerical study of shear-relative low-level mean flow on tropical cyclone intensity and size. *Journal of the Atmospheric Sciences*, 76, 2309–2334. <https://doi.org/10.1175/JAS-D-18-0315.1>
- Czajkowski, J., & Done, J. (2014). As the wind blows? Understanding hurricane damages at the local level through a case study analysis. *Weather, Climate, and Society*, 6(2), 202–217. <https://doi.org/10.1175/WCAS-D-13-00024.1>
- Dai, A. (2006). Recent climatology, variability, and trends in global surface humidity. *Journal of Climate*, 19(15), 3589–3606. <https://doi.org/10.1175/JCLI3816.1>
- Davis, C. A., & Ahijevych, D. A. (2013). Thermodynamic environments of deep convection in Atlantic tropical disturbances. *Journal of the Atmospheric Sciences*, 70, 1912–1928. <https://doi.org/10.1175/JAS-D-12-0278.1>
- Davis, C. A., & Galarraga, T. J. (2009). The vertical structure of mesoscale convective vortices. *Journal of the Atmospheric Sciences*, 66, 686–704. <https://doi.org/10.1175/2008JAS2819.1>
- Doyle, J. D., Moskaitis, J. R., Feldmeier, J. W., Ferek, R. J., Beaubien, M., Bell, M. M., et al. (2017). A view of tropical cyclones from above: The Tropical Cyclone Intensity (TCI) experiment. *Bulletin of the American Meteorological Society*, 98, 2113–2134. <https://doi.org/10.1175/BAMS-D-16-0055.1>
- Dunion, J. P. (2011). Rewriting the climatology of the tropical North Atlantic and Caribbean Sea atmosphere. *Journal of Climate*, 24, 893–908. <https://doi.org/10.1175/2010JCLI3496.1>
- Dunkerton, T. J., Montgomery, M. T., & Wang, Z. (2009). Tropical cyclogenesis in a tropical wave critical layer: Easterly waves. *Atmospheric Chemistry and Physics*, 9, 5587–5646. <https://doi.org/10.5194/acp-9-5587-2009>
- Dunnavan, G. M., & Diercks, J. W. (1980). An analysis of super typhoon tip (October 1979). *Monthly Weather Review*, 108, 1915–1923. [https://doi.org/10.1175/1520-0493\(1980\)108<1915:AOOSTT>2.0.CO;2](https://doi.org/10.1175/1520-0493(1980)108<1915:AOOSTT>2.0.CO;2)
- Fovell, R. G., Bu, Y. P., Corbosiero, K. L., Tung, W., Cao, Y., Kuo, H., et al. (2016). Influence of cloud microphysics and radiation on tropical cyclone structure and motion. *Meteorological Monographs*, 56, 11.1–11.27. <https://doi.org/10.1175/AMSMONOGRAPH-D-15-0006.1>
- Gray, W. H. (1968). Global view of the origin of tropical disturbances and storms. *Monthly Weather Review*, 96, 669–700.
- Harr, P. A., Kalafsky, M. S., & Elsberry, R. L. (1996). Environmental conditions prior to formation of a midget tropical cyclone during TCM-93. *Monthly Weather Review*, 116, 1693–1710. [https://doi.org/10.1175/1520-0493\(1996\)124<1693:ECPTFO>2.0.CO;2](https://doi.org/10.1175/1520-0493(1996)124<1693:ECPTFO>2.0.CO;2)
- Hawkins, H. F., & Imbembo, S. M. (1976). The structure of a small, intense hurricane—Inez 1966. *Monthly Weather Review*, 104, 418–442. [https://doi.org/10.1175/1520-0493\(1976\)104<0418:TSOASI>2.0.CO;2](https://doi.org/10.1175/1520-0493(1976)104<0418:TSOASI>2.0.CO;2)
- Hawkins, H. F., & Rubsam, D. T. (1966). Hurricane Inez—A classic “micro-hurricane”. *Mariners Weather Log*, 11, 157–160.
- Hence, D. A., & Houze, R. A. (2012). Vertical structure of tropical cyclone rainbands as seen by the TRMM precipitation radar. *Journal of the Atmospheric Sciences*, 69, 2644–2661. <https://doi.org/10.1175/JAS-D-11-0323.1>
- Hill, K. A., & Lackmann, G. M. (2009). Influence of environmental humidity on tropical cyclone size. *Monthly Weather Review*, 137, 3294–3315. <https://doi.org/10.1175/2009MWR2679.1>
- Holloway, C. E., & Neelin, J. D. (2009). Moisture vertical structure, column water vapor, and tropical deep convection. *Journal of the Atmospheric Sciences*, 66, 1665–1683. <https://doi.org/10.1175/2008JAS2806.1>
- Houze, R. A. (2010). Clouds in tropical cyclones. *Monthly Weather Review*, 138, 293–344. <https://doi.org/10.1175/2009MWR2989.1>

- Judit, F., & Chen, S. S. (2016). Predictability and dynamics of tropical cyclone rapid intensification deduced from high-resolution stochastic ensembles. *Monthly Weather Review*, 144, 4395–4420. <https://doi.org/10.1175/MWR-D-15-0413.1>
- Kaplan, J., DeMaria, M., & Knaff, J. A. (2010). A revised tropical cyclone rapid intensification index for the Atlantic and eastern North Pacific basins. *Weather and Forecasting*, 25, 220–241. <https://doi.org/10.1175/2009WAF2222280.1>
- Kepert, J. D. (2012). Choosing a boundary layer parameterization for tropical cyclone modeling. *Monthly Weather Review*, 140, 1427–1445. <https://doi.org/10.1175/MWR-D-11-00217.1>
- Kilroy, G., & Smith, R. K. (2017). The effects of initial vortex size on tropical cyclogenesis and intensification. *Quarterly Journal of the Royal Meteorological Society*, 143, 2832–2845. <https://doi.org/10.1002/qj.3134>
- Kimball, S. K., & Mulekar, M. S. (2004). A 15-year climatology of North Atlantic tropical cyclones. Part I: Size parameters. *Journal of Climate*, 17, 3555–3575. [https://doi.org/10.1175/1520-0442\(2004\)017<3555:AYCONA>2.0.CO;2](https://doi.org/10.1175/1520-0442(2004)017<3555:AYCONA>2.0.CO;2)
- Klotzbach, P. J., Bell, M. M., Bowen, S. G., & Gibney, E. J. (2020). Surface pressure a more skillful predictor of normalized hurricane damage than maximum sustained wind. *Bulletin of the American Meteorological Society*, 101, E830–E846. <https://doi.org/10.1175/BAMS-D-19-0062.1>
- Klotzbach, P. J., Bowen, S. G., Pielke, R. A., & Bell, M. M. (2018). Continental U.S. hurricane landfall frequency and associated damage: Observations and future risks. *Bulletin of the American Meteorological Society*, 99, 1359–1376. <https://doi.org/10.1175/BAMS-D-17-0184.1>
- Knaff, J. A., Longmore, S. P., & Molenar, D. A. (2014). An objective satellite-based tropical cyclone size climatology. *Journal of Climate*, 27, 455–476. <https://doi.org/10.1175/JCLI-D-13-00096.1>
- Knaff, J. A., Sampson, C. R., & Chirokova, G. (2017). A global statistical-dynamical tropical cyclone wind radii forecast scheme. *Weather and Forecasting*, 32, 629–644. <https://doi.org/10.1175/WAF-D-16-0168.1>
- Knutson, T. R., Sirutis, J. J., Zhao, M., Tuleya, R. E., Bender, M., Vecchi, G. A., et al. (2015). Global projections of intense tropical cyclone activity for the late twenty-first century from dynamical downscaling of CMIP5/RCP4.5 scenarios. *Journal of Climate*, 28, 7203–7224. <https://doi.org/10.1175/JCLI-D-15-0129.1>
- Komaromi, W. A. (2013). An investigation of composite dropsonde profiles for developing and nondeveloping tropical waves during the 2010 PREDICT field campaign. *Journal of the Atmospheric Sciences*, 70, 542–558. <https://doi.org/10.1175/JAS-D-12-052.1>
- Liu, K. S., & Chan, J. C. L. (2002). Synoptic flow patterns associated with small and large tropical cyclones over the western North Pacific. *Monthly Weather Review*, 130, 2134–2142. [https://doi.org/10.1175/1520-0493\(2002\)130<2134:SFPAWS>2.0.CO;2](https://doi.org/10.1175/1520-0493(2002)130<2134:SFPAWS>2.0.CO;2)
- Louis, J. F. (1979). A parametric model of vertical eddy fluxes in the atmosphere. *Boundary-Layer Meteorology*, 17, 187–202. <https://doi.org/10.1007/BF00117978>
- Mallen, K. J., Montgomery, M. T., & Wang, B. (2005). Reexamining the near-core radial structure of the tropical cyclone primary circulation: Implications for vortex resiliency. *Journal of the Atmospheric Sciences*, 62, 408–425. <https://doi.org/10.1175/JAS-3377.1>
- Martinez, J., Bell, M. M., Rogers, R. F., & Doyle, D. J. (2019). Axisymmetric potential vorticity evolution of Hurricane Patricia (2015). *Journal of the Atmospheric Sciences*, 76, 2043–2063. <https://doi.org/10.1175/JAS-D-18-0373.1>
- McTaggart-Cowan, R., Deane, G. D., Bosart, L. F., Davis, C. A., & Galarneau, T. J. (2008). Climatology of tropical cyclogenesis in the North Atlantic (1948–2004). *Monthly Weather Review*, 136, 1284–1304. <https://doi.org/10.1175/2007MWR2245.1>
- McTaggart-Cowan, R., Galarneau, T. J., Bosart, L. F., Moore, R. W., & Martius, O. (2013). A global climatology of baroclinically influenced tropical cyclogenesis. *Monthly Weather Review*, 141(6), 1963–1989. <https://doi.org/10.1175/MWR-D-12-00186.1>
- Merrill, R. T. (1984). A comparison of large and small tropical cyclones. *Monthly Weather Review*, 112, 1408–1418. [https://doi.org/10.1175/1520-0493\(1984\)112<1408:ACOLAS>2.0.CO;2](https://doi.org/10.1175/1520-0493(1984)112<1408:ACOLAS>2.0.CO;2)
- Musgrave, K. D., Taft, J. L., McNoldy, B. D., & Schubert, W. H. (2012). Time evolution of the intensity and size of tropical cyclones. *Journal of Advances in Modeling Earth Systems*, 4, M08001. <https://doi.org/10.1029/2011MS000104>
- Nguyen, L. T., Molinari, J., & Thomas, D. (2014). Evaluation of tropical cyclone center identification methods in numerical models. *Monthly Weather Review*, 142, 4326–4339. <https://doi.org/10.1175/MWR-D-14-00044.1>
- Nolan, D. S. (2007). What is the trigger for tropical cyclogenesis? *Australian Meteorological Magazine*, 56, 241–266.
- Onderlinde, M. J., & Nolan, D. S. (2017). The tropical cyclone response to changing wind shear using the method of time-varying point-downscaling. *Journal of Advances in Modeling Earth Systems*, 9, 908–931. <https://doi.org/10.1002/2016MS000796>
- Powell, M., & Reinhold, T. (2007). Tropical cyclone destructive potential by integrated kinetic energy. *Bulletin of the American Meteorological Society*, 88, 513–526. <https://doi.org/10.1175/BAMS-88-4-513>
- Raymond, D. J., Sessions, S. L., & Carrillo, C. L. (2011). Thermodynamics of tropical cyclogenesis in the northwest Pacific. *Journal of Geophysical Research*, 116, D18101. <https://doi.org/10.1029/2011JD015624>
- Rios-Berrios, R., Davis, C. A., & Torn, R. D. (2018). A hypothesis for the intensification of tropical cyclones under moderate vertical wind shear. *Journal of the Atmospheric Sciences*, 75, 4149–4173. <https://doi.org/10.1175/JAS-D-18-0070.1>
- Rios-Berrios, R., Torn, R. D., & Davis, C. A. (2016). An ensemble approach to investigate tropical cyclone intensification in sheared environments. Part I: Katia (2011). *Journal of the Atmospheric Sciences*, 73, 71–93. <https://doi.org/10.1175/JAS-D-15-0052.1>
- Rogers, R. F., Aberson, S., Bell, M. M., Cecil, D. J., Doyle, J. D., Kimberlain, T. B., et al. (2017). Re-writing the tropical record books: The extraordinary intensification of Hurricane Patricia (2015). *Bulletin of the American Meteorological Society*, 98, 2091–2112. <https://doi.org/10.1175/BAMS-D-16-0039.1>
- Rotunno, R., & Emanuel, K. A. (1987). An air-sea interaction theory for tropical cyclones. Part II: Evolutionary study using a nonhydrostatic axisymmetric numerical model. *Journal of the Atmospheric Sciences*, 44, 542–561. [https://doi.org/10.1175/1520-0469\(1987\)044<042:AAITFT>2.0.CO;2](https://doi.org/10.1175/1520-0469(1987)044<042:AAITFT>2.0.CO;2)
- Rozoff, C. M., Schubert, W. H., & McNoldy, B. D. (2006). Rapid filamentation zones in intense tropical cyclones. *Journal of the Atmospheric Sciences*, 63, 325–340. <https://doi.org/10.1175/JAS3595.1>
- Schenkel, B., Lin, N., Chavas, D., Vecchi, G. A., Knutson, T. R., & Oppenheimer, M. (2018). Will outer tropical cyclone size change due to anthropogenic warming? 33rd Conference on Hurricanes and Tropical Meteorology, Jacksonville, FL, Amer. Meteor. Soc., <https://ams.confex.com/ams/33HURRICANE/webprogram/Paper339539.html>
- Schenkel, B. A., Lin, N., Chavas, D., Vecchi, G. A., Oppenheimer, M., & Brammer, A. (2018). Lifetime evolution of outer tropical cyclone size and structure as diagnosed from reanalysis and climate model data. *Journal of Climate*, 31, 7985–8004. <https://doi.org/10.1175/JCLI-D-17-0630.1>
- Tao, D., Bell, M., Rotunno, R., & van Leeuwen, P. J. (2020). Why do the maximum intensities in modeled tropical cyclones vary under the same environmental conditions? *Geophysical Research Letters*, 47, e2019GL085980. <https://doi.org/10.1029/2019GL085980>

- Tao, D., & Zhang, F. (2014). Effect of environmental shear, sea-surface temperature, and ambient moisture on the formation and predictability of tropical cyclones: An ensemble-mean perspective. *Journal of Advances in Modeling Earth Systems*, 6, 384–404. <https://doi.org/10.1002/2014MS000314>
- Terwey, W. D., & Rozoff, C. M. (2014). Objective convective updraft identification and tracking: Part 1. Structure and thermodynamics of convection in the rainband regions of two hurricane simulations. *Journal of Geophysical Research: Atmospheres*, 119, 6470–6496. <https://doi.org/10.1002/2013JD020904>
- Van Sang, N., Smith, R. K., & Montgomery, M. T. (2008). Tropical-cyclone intensification and predictability in three dimensions. *Quarterly Journal of the Royal Meteorological Society*, 134, 563–582. <https://doi.org/10.1002/qj.235>
- Wang, S., & Toumi, R. (2016). On the relationship between hurricane cost and the integrated wind profile. *Environmental Research Letters*, 11, 114,005. <https://doi.org/10.1088/1748-9326/11/11/114005>
- Wang, S., & Toumi, R. (2019). Impact of dry midlevel air on the tropical cyclone outer circulation. *Journal of the Atmospheric Sciences*, 76, 1809–1826. <https://doi.org/10.1175/JAS-D-18-0302.1>
- Weatherford, C. L., & Gray, W. M. (1988). Typhoon structure as revealed by aircraft reconnaissance. Part II: Structural variability. *Monthly Weather Review*, 116, 1044–1056. [https://doi.org/10.1175/1520-0493\(1988\)116<1044:TSARBA>2.0.CO;2](https://doi.org/10.1175/1520-0493(1988)116<1044:TSARBA>2.0.CO;2)
- Xu, J., & Wang, Y. (2010). Sensitivity of the simulated tropical cyclone inner-core size to the initial vortex size. *Monthly Weather Review*, 138, 4135–4157. <https://doi.org/10.1175/2010MWR3335.1>
- Xu, J., & Wang, Y. (2018). Effect of the initial vortex structure on intensification of a numerically simulated tropical cyclone. *Journal of the Meteorological Society of Japan*, 96, 111–126. <https://doi.org/10.2151/jmsj.2018-014>
- Zhai, A. R., & Jiang, H. J. (2014). Dependence of U.S. hurricane economic loss on maximum wind speed and storm size. *Environmental Research Letters*, 9, 064019. <https://doi.org/10.1088/1748-9326/9/6/064019>